AGU PUBLICATIONS

JGR

Journal of Geophysical Research: Atmospheres

RESEARCH ARTICLE
10.1002/2016JD024787

Key Points:
- Simultaneously fitting cloud and aerosol allows for aerosol retrievals closer to clouds
- Three-dimensional effects need to be taken into account to improve aerosol retrievals near clouds

Correspondence to:
O. P. Hasekamp,
O.Hasekamp@sron.nl

Citation:
Stap, F. A., O. P. Hasekamp, C. Emde, and T. Röckmann (2016), Multiangle photopolarimetric aerosol retrievals in the vicinity of clouds: Synthetic study based on a large eddy simulation, *J. Geophys. Res. Atmos.*, *121*, 12,914–12,935, doi:10.1002/2016JD024787.

Received 11 JAN 2016
Accepted 19 SEP 2016
Accepted article online 24 SEP 2016
Published online 5 NOV 2016

©2016. American Geophysical Union. All Rights Reserved.

Multiangle photopolarimetric aerosol retrievals in the vicinity of clouds: Synthetic study based on a large eddy simulation

F. A. Stap[1,2], O. P. Hasekamp[1], C. Emde[3], and T. Röckmann[2]

[1]SRON Netherlands Institute for Space Research, Utrecht, Netherlands, [2]Institute for Marine and Atmospheric Research, Utrecht University, Utrecht, Netherlands, [3]Meteorological Institute, Ludwig-Maximilians University, Munich, Germany

Abstract We investigate the effect of cloud contamination and 3-D radiative transfer effects on aerosol retrievals from multiangle photopolarimetric measurements in the vicinity of clouds. To this end multiangle, multiwavelength photopolarimetric observations are simulated using a 3-D radiative transfer model for scenes with realistic cloud properties, based on a large eddy simulation. Spatial resolutions of 2×2, 4×4, and 6×6 km^2 have been considered. It is found that a goodness-of-fit criterion efficiently filters out cloud contamination. However, it does not filter out all scenes that are affected by 3-D radiative effects, resulting in small biases in the retrieved aerosol optical thickness (AOT) and single-scattering albedo (SSA). We also found that measurements at higher spatial resolution (2×2 km^2) do not result in retrievals closer to clouds compared to measurements at coarser spatial resolutions (4×4 and 6×6 km^2). If cloud parameters are fitted simultaneously with aerosol parameters using a 1-D radiative transfer model and the Independent Pixel Approximation, more successful retrievals are obtained in partially cloudy scenes and in the vicinity of clouds. This effect is most apparent at 6×6 km^2 and only marginal at 2×2 km^2 resolution. The retrieved aerosol AOT and SSA from the simultaneous aerosol and cloud retrievals still have a small bias, like the aerosol-only retrievals. We conclude that in order to substantially improve aerosol retrievals in the vicinity of clouds, a retrieval algorithm is needed that takes into account 3-D radiative transfer effects.

1. Introduction

Aerosols affect the climate directly by absorbing and scattering incoming solar radiation and indirectly by changing the macrophysical and microphysical properties of clouds. The aerosol radiative forcing represents the most uncertain factor in the most recent Intergovernmental Panel on Climate Change assessment [*Boucher et al.*, 2013]. Aerosols can affect cloud properties in various ways, as described, e.g., in the review paper by *Lohmann and Feichter* [2005]. The first indirect effect, referred to as the "Twomey effect" or "cloud albedo effect," is the effect that an increase in aerosol concentration leads to a cloud that has more but smaller cloud droplets, which results in a higher reflectivity of the cloud [*Twomey*, 1959]. The second aerosol indirect effect is the effect that smaller cloud droplets (due to more aerosol particles competing for the same amount of water vapor) decrease the precipitation efficiency which results in a prolonged cloud lifetime [*Albrecht*, 1989]. A number of studies have used satellite observations to study the effects of aerosols on cloud properties and estimate the radiative forcing due to the first and, sometimes also, the second indirect aerosol effects [*Bréon et al.*, 2002; *Lohmann and Lesins*, 2002; *Sekiguchi et al.*, 2003; *Quaas et al.*, 2006, 2008; *Bellouin et al.*, 2013]. These studies confirm that the number concentration of aerosol particles negatively correlates with the cloud droplet radius and positively correlates with cloud optical thickness and cloud fraction.

A limiting factor for satellite studies of the indirect aerosol radiative effect is that aerosol retrievals may be biased for scenes in between and near clouds, because there can be undetected cloud contamination [*Koren et al.*, 2007; *Charlson et al.*, 2007; *Redemann et al.*, 2009] as well as 3-D radiative transfer effects [*Wen et al.*, 2007; *Várnai and Marshak*, 2009] (e.g., shadows and cloud-induced reflectance enhancements in the cloud-free columns).

From a passive remote sensing point of view, the largest amount of aerosol information can be provided by instruments that measure intensity and polarization of backscattered/reflected light at multiple viewing angles over a broad wavelength range. This has been demonstrated in several theoretical studies

21698996, 2016, 21, Downloaded from https://agupubs.onlinelibrary.wiley.com/doi/10.1002/2016JD024787, Wiley Online Library on [24/02/2025]. See the Terms and Conditions (https://onlinelibrary.wiley.com/terms-and-conditions) on Wiley Online Library for rules of use; OA articles are governed by the applicable Creative Commons License

[*Mishchenko and Travis*, 1997; *Hasekamp and Landgraf*, 2007; *Kokhanovsky et al.*, 2010; *Knobelspiesse et al.*, 2012; *Ottaviani et al.*, 2013] as well as case studies using airborne measurements [*Chowdhary et al.*, 2005; *Waquet et al.*, 2009; *Wu et al.*, 2015]. Due to the different angular light-scattering properties between aerosols and cloud droplets, in particular for polarization, multiangle measurements of intensity and polarization also have the potential to separate aerosol scattering and cloud scattering. This feature has been used by *Stap et al.* [2015] to screen for clouds in POLDER-3/PARASOL observations. With an adequate goodness-of-fit criterion, combined with a filter for ice clouds, they are able to filter liquid water cloud contamination and find that fewer high aerosol load scenes are falsely flagged as cloudy than when using a cloud mask from Moderate Resolution Imaging Spectroradiometer.

A logical next step is to retrieve aerosol and cloud properties simultaneously in scenes with partial liquid water cloud cover. This approach was suggested by *Hasekamp* [2010] based on a synthetic study using a 1-D radiative transfer (RT) model. A complication that arises when one wants to analyze observations that are partially clouded or in the vicinity of clouds is that measurements are affected by 3-D effects such as shadows and cloud-induced reflectance enhancements in the cloud-free columns. *Stap et al.* [2016] investigated the influence of 3-D radiative effects on 1-D simultaneous aerosol and cloud retrievals in scenes with partial liquid water cloud cover from multiangle, multiwavelength photopolarimetric measurements in a generic set of synthetic observations for 3-D RT models with cuboid clouds. The study shows that aerosol parameters can be determined with sufficient accuracy in observations with cloud cover in the range of 2–20% and low optical thickness ($\tau^{\text{cloud}}_{550\,\text{nm}} \leq 10.0$), where the retrieval errors are highly dependent on the type of cloud distribution. At too high optical thickness or cloud fraction the 3-D radiative effects lead to substantial errors in the retrieved aerosol properties.

In this paper we build on the studies of *Stap et al.* [2015, 2016] focusing on the following new questions:

1. What is the capability of aerosol-only retrievals from multiangle photopolarimetric measurements to provide aerosol information in the vicinity of clouds?
2. Can aerosol retrievals in the vicinity of clouds be improved (in terms of accuracy and distance to clouds) when cloud properties are fitted simultaneously with aerosol properties?
3. What is the benefit of improved spatial resolution for aerosol retrievals in the vicinity of clouds?

To answer these questions, we use a 3-D radiative transfer model to create synthetic multiangle, multiwavelength measurements of intensity and polarization for a generic satellite instrument in two realistic, partially clouded scenes based on a large eddy simulation (LES). From these synthetic measurements we perform aerosol-only retrievals and simultaneous aerosol-cloud retrievals using a 1-D radiative transfer model.

The paper is organized as follows: the simulated measurements, the modeling of the cloud distribution, the 3-D RT code, and the retrieval algorithm are described in section 2. In section 3 the influence of cloud contamination and 3-D radiative effects are analyzed and the results of the two types of retrievals are presented (with and without clouds, respectively). The results and conclusions of this paper are discussed in section 4.

2. Methods

We first present the multiangle, multiwavelength observations that are simulated in section 2.1. Then, in section 2.2, we describe how the realistic clouds are modeled by using cloud distributions from a LES. The 3-D RT code and its setup are described in section 2.3. A short summary of the inversion algorithm for aerosol-only retrieval and simultaneous aerosol and cloud retrieval is given in section 2.4.

2.1. Simulated Measurements

Multiwavelength, multiviewing-angle synthetic observations are simulated for a generic instrument that observes intensity and degree of linear polarization in six bands: 410.0, 491.5, 669.9, 863.4, 1019.4, and 1600.0 nm, at 15 viewing zenith angles (VZA, θ_{sat}) and three spatial resolutions: 2×2, 4×4, and 6×6 km^2. The satellite moves from $\theta_{\text{sat}} = 63°$ and the satellite azimuth angle $\phi_{\text{sat}} = 180°$ (measured clockwise with respect to the north), through zenith to $\theta_{\text{sat}} = 63°$ and $\phi_{\text{sat}} = 0°$ in steps of 9°. In all models the Sun is positioned in the southwest; $\phi_{\text{sun}} = 20°$ (the solar azimuth angle counted clockwise starting from the south). Two solar zenith angles (SZAs) are explored ($\theta_{\text{sun}} = 40°$ and $\theta_{\text{sun}} = 60°$). Therefore, the synthetic observations have scattering angle ranges from 79° to 167° and from 60° to 162° for, respectively, $\theta_{\text{sun}} = 40°$ and $\theta_{\text{sun}} = 60°$.

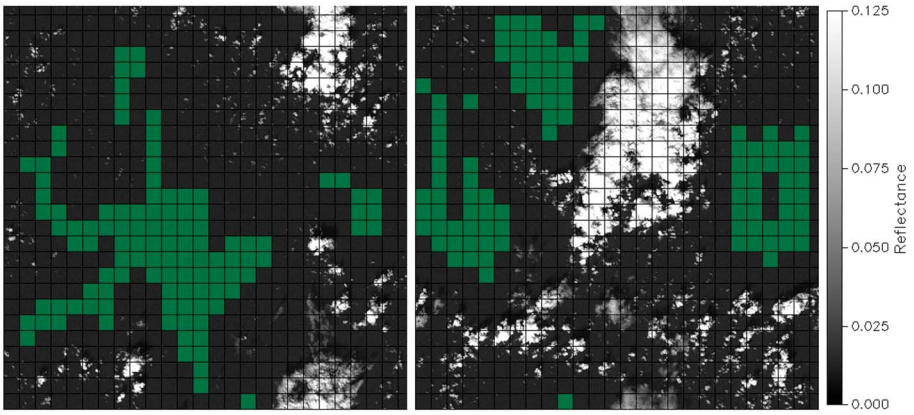

Figure 1. The reflectance at 670 nm in a black and white scale for the cloud distribution of (left) case A and (right) case B with the fine absorbing aerosol (see Table 1) distributed below the clouds. A black grid indicates the 2×2 km^2 ground pixels. The ground pixels of measurements that are completely cloud free at all VZA are indicated in green. The Sun is positioned in the southwest ($\phi_{sun} = 20°$, counted clockwise starting from the south) at SZA = 40° . The domain of both images is 51.2×51.2 km^2.

2.2. Modeling of Realistic Clouds

Cloud water distributions are taken from simulations of shallow trade wind cumuli in the western Atlantic Ocean by *Seifert and Heus* [2013] who applied the University of California LES code [*Stevens et al.*, 1999, 2005; *Stevens and Seifert*, 2008] to initial meteorological conditions observed in the Rain In Cumulus over the Ocean (RICO) field campaign [*Rauber et al.*, 2007]. The model assumes a constant droplet number concentration of 70 cm^{-3} and simulates the total water, cloud water, and rainwater mass mixing ratios as well as the rain number concentration, the pressure, and liquid water potential temperature with a spatial resolution of $25 \times 25 \times 25$ m^3 on a domain of $51.2 \times 51.2 \times 5.0$ km^3 for a duration of 60 h. Note that the domain height and running time of the simulation used in this study are larger than the simulation presented in *Seifert and Heus* [2013]. For more details on the LES simulation the reader is referred to *Seifert and Heus* [2013].

The 3-D cloud distribution in the 3-D RT code setup uses the liquid water content (LWC) and droplet size distribution. Here we describe how these variables are derived from the LES output. The cloud distributions at two moments in time of the LES are selected on the availability of cloud-free observations in the domain, cases A and B as shown in Figure 1. For simplicity we decided to only use the liquid water that makes up the clouds and ignore the liquid water in the form of rain (i.e., we take the liquid water mixing ratio to be equal to the cloud water mixing ratio). In order to calculate the liquid water content (LWC), we first approximate the potential temperature (θ, in K) of the parcel of air from the liquid water potential temperature (θ_L, in K) and liquid water mixing ratio (r_L, in g/kg) given by the LES:

$$\theta \approx \theta_L + \frac{L_v}{c_p} r_L \tag{1}$$

using the latent heat of vaporization (L_v, in J/g) and the specific heat of dry air at constant pressure (c_p in J/kg/K). Then we calculate the temperature of the parcel of air (T, in K) under the assumption that the parcel has been adiabatically lifted from standard pressure ($p_0 = 1000$ hPa) to its current height using the pressure (p, in Pa) provided by the LES:

$$T = \theta \left(\frac{p}{p_0} \right)^{\frac{R}{M_{air} c_p}} \tag{2}$$

where R is the gas constant (in J/mol/K) and M_{air} is the molar mass of dry air (in kg/mol). Now the LWC can be calculated (in g/m^3) from the liquid water mixing ratio and temperature, using the ideal gas law, as the following:

$$\mathrm{LWC} = r_L \frac{M_{air} p}{RT} \tag{3}$$

Because of computational efficiency, the LWC has been smoothed to a slightly lower resolution of $50 \times 50 \times 50$ m^3.

21698996, 2016, 21, Downloaded from https://agupubs.onlinelibrary.wiley.com/doi/10.1002/2016JD024787, Wiley Online Library on [24/02/2025]. See the Terms and Conditions (https://onlinelibrary.wiley.com/terms-and-conditions) on Wiley Online Library for rules of use; OA articles are governed by the applicable Creative Commons License

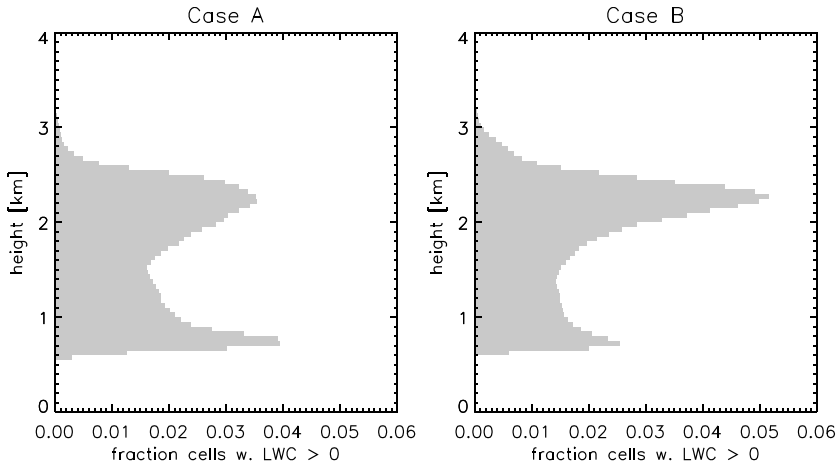

Figure 2. The vertical distribution of grid cells containing liquid water droplets for cases A and B. The vertical resolution of the grid is 50 m. A cutoff on the LWC is applied for the sample grid cells with LWC $< 0.0057 g/cm^3$, as it can be argued that these amounts of liquid water would result in hydrated aerosol rather than cloud droplets. This cutoff results in a lower limit for the cloud droplet effective radius ($r_{\text{eff}}^{\text{cloud}} \geq 3.0$ μm). In case A there is a total of 2.8×10^7 kg liquid water versus 8.5×10^7 kg in case B.

A gamma size distribution with effective variance of $v_{\text{eff}} = 0.1$ is assumed for the cloud droplets following *Hansen and Travis* [1974]:

$$n(r) = r^{\frac{(1-3v_{\text{eff}})}{v_{\text{eff}}}} e^{-\left(\frac{r}{r_{\text{eff}} v_{\text{eff}}}\right)} \tag{4}$$

where r_{eff} is the effective radius and n is the number of particles of radius r. The LWC and the size distribution are related as follows:

$$\text{LWC} = \rho N \frac{\int n(r) \frac{4}{3} \pi r^3 \mathrm{d}r}{\int n(r) \mathrm{d}r} \tag{5}$$

where ρ is the mass density of water, N is the droplet number concentration ($N = 70$ cm^{-3}), and the integral in the numerator describes the total volume of all droplets in the size distribution and is normalized by the integral in the denominator. Now we can calculate the effective radius of the cloud droplets for a certain LWC using equations (4) and (5). The effective radii of the cloud droplets range between 3 and 24 μm, and the resulting clouds are distributed between 0.5 and 3.5 km (see Figure 2). Finally, the optical properties that are needed as input to the core radiative transfer code (optical thickness, SSA, and phase matrix) are calculated using a Mie code.

2.3. The MYSTIC 3-D Radiative Transfer Code

The 3-D radiative transfer code MYSTIC (Monte Carlo for the physically correct tracing of photons in cloudy atmospheres) [*Mayer*, 2009; *Emde and Mayer*, 2007; *Emde et al.*, 2010] is one of the solvers of the radiative transfer equations in libRadtran [*Emde et al.*, 2016]. The code traces photons as they enter the scene until they are absorbed or leave the scene. The "local estimate method" [*Marshak and Davis*, 2005] and the "variance reduction optimal options method" [*Buras and Mayer*, 2011] are applied to optimize the algorithm in terms of computational efficiency.

The model has periodic boundary conditions in the vertical planes (i.e., a photon that crosses the northern boundary will reenter the scene at the southern boundary). The values for the four stokes parameters are stored on a 50×50 m^2 sample grid at the top of the atmosphere. A black surface is used.

Simulations are run for the aerosol types (see Table 1); type A is representative of fine absorbing aerosol which has a high aerosol load and absorption, type B is representative for coarse nonspherical aerosol which has a lower load, and finally, for some selected simulations an aerosol type C has been used that is practically nonabsorbing and is further the same as aerosol type A. For the coarse nonspherical aerosol type

21698996, 2016, 21, Downloaded from https://agupubs.onlinelibrary.wiley.com/doi/10.1002/2016JD024787, Wiley Online Library on [24/02/2025]. See the Terms and Conditions (https://onlinelibrary.wiley.com/terms-and-conditions) on Wiley Online Library for rules of use; OA articles are governed by the applicable Creative Commons License

21698996, 2016, 21, Downloaded from https://agupubs.onlinelibrary.wiley.com/doi/10.1002/2016JD024787, Wiley Online Library on [24/02/2025]. See the Terms and Conditions (https://onlinelibrary.wiley.com/terms-and-conditions) on Wiley Online Library for rules of use; OA articles are governed by the applicable Creative Commons License

Table 1. The Optical and Microphysical Parameters for the Three Aerosol Cases: Fine Absorbing (Type A), Coarse Nonspherical (Type B), and Fine Nonabsorbing (Type C)[a]

	Fine Absorbing	Coarse Nonspherical	Fine Nonabsorbing
$\tau^{f}_{550\,nm}$	0.738	0.042	0.738
$\tau^{c}_{550\,nm}$	0.062	0.118	0.062
r^{f}_{eff} (μm)	0.119	0.105	0.119
v^{f}_{eff}	0.174	0.323	0.174
m^{f}_{r}	1.50	1.53	1.50
m^{f}_{i}	−0.020	−0.0055	1.0E−5
r^{c}_{eff} (μm)	2.671	1.605	2.671
v^{c}_{eff}	0.704	0.418	0.704
m^{c}_{r}	1.50	1.53	1.50
m^{c}_{i}	−0.020	−0.0055	1.0E−5
Sph[c]	1.00	0.10	1.00

[a]The table lists the AOT of each mode ($\tau_{550\,nm}$), where superscripts f and c indicate fine or coarse mode, followed by the effective radius (r_{eff}), effective variance (v_{eff}), the real and imaginary part of the complex refractive index (m_r and m_i), and (for the coarse mode only) a fraction of spherical particles (Sph).

we use the approach proposed by *Dubovik et al.* [2006] assuming a mixture of spheres and spheroids with a fixed aspect ratio distribution. For all cases the aerosol is homogeneously distributed below the clouds between 0 and 700 m. Note that this almost completely separates the aerosol from the clouds; less than 0.9% and 0.4% of all the LWC is below 700 m for, respectively, the cases A and B. Note that the aerosols are not humidified according to the modeled water vapor distribution, as would be the case in a realistic scene.

The scattering and absorption properties of air molecules as a function of wavelength are specified in 20 vertical layers between 0.0 and 40.0 km. For liquid water droplets these properties are provided on a $50 \times 50 \times 50$ m^3 grid.

The three spatial resolutions (2×2, 4×4, and 6×6 km^2) are simulated by averaging over the appropriate pixels of the MYSTIC sample grid (which has a resolution of 50×50 m^2). The size of the satellite ground pixel and the number of photons determine the uncertainty in the reflectances calculated by MYSTIC, which occur due to the statistical nature of the Monte Carlo method. This, so-called, photon noise is largest for the highest-resolution synthetic measurements (i.e., for 2×2 km^2 resolution). At this resolution the mean relative uncertainty in reflectance of every synthetic measurement is smaller than 0.5%, while the mean absolute uncertainty in the Degree of Linear Polarization (DoLP) is smaller than 0.0035.

2.4. Inversion Algorithm

The algorithm for retrieving aerosol properties from multiangle, photopolarimetric measurements that is applied in this study is based on *Hasekamp et al.* [2011]. The algorithm works by iteratively fitting a (1-D) linearized vector RT model [*Landgraf et al.*, 2001; *Hasekamp and Landgraf*, 2002, 2005] to the observation, where at every iteration an adjustment to the fit parameters is chosen using Philips-Tikhonov regularization. The fit parameters correspond to the microphysical aerosol properties of a fine and a coarse mode. Both modes have a lognormal size distribution described by an effective radius, effective variance, complex refractive indices, a column number concentration, and, for the coarse mode only, the fraction of spherical particles (using precalculated kernels of optical properties by *Dubovik et al.* [2006]). When the retrieval has converged, the quality of the fit is quantified by calculating a χ^2;

$$\chi^2 = \frac{1}{n}\sum_{i}^{n}\frac{\left(F_i^{meas} - F_i^{model}\right)^2}{\sigma_i^2}, \tag{6}$$

where F_i^{meas} is an element of the measurements vector, F_i^{model} is an element of the forward model vector, σ is the measurement uncertainty, and n is the number of elements in state vectors F_i^{meas} and F_i^{model}.

21698996, 2016, 21, Downloaded from https://agupubs.onlinelibrary.wiley.com/doi/10.1002/2016JD024787, Wiley Online Library on [24/02/2025]. See the Terms and Conditions (https://onlinelibrary.wiley.com/terms-and-conditions) on Wiley Online Library for rules of use; OA articles are governed by the applicable Creative Commons License

Table 2. Summary of the Parameters That are Retrieved for the Two Types of Retrievals That Are Used in This Study[a]

	Aerosol Only	Aerosol and Cloud
Aerosol parameters	r_{eff} (μm)	r_{eff} (μm)
	v_{eff}	v_{eff}
	m_{r}	m_{r}
	m_{i}	m_{i}
	n_{col}	n_{col}
	Sph (coarse mode only)	Sph (coarse mode only)
Cloud parameters		n_{col}
		f

[a]The aerosol parameters consist of the effective radius (r_{eff}), effective variance (v_{eff}), the real and imaginary part of the complex refractive index (m_{r} and m_{i}), the column-integrated number of particles (n_{col}) and a fraction of spherical particles (Sph). The cloud parameters have the coverage fraction (f) as additional retrieval parameter.

Stap et al. [2016] extended the retrieval algorithm and RT code to include partial, liquid water cloud cover using the Independent Pixel Approximation (IPA):

$$\vec{I}_{\text{IPA}} = (1 - f)\vec{I}_{\text{clear}} + f\vec{I}_{\text{cloud}}, \tag{7}$$

where f is the cloud fraction and $\vec{I}$ is the intensity vector that has the Stokes parameters as its components, while subscripts "clear" and "cloud" denote, respectively, a cloud-free atmosphere and a fully clouded atmosphere. The cloud is described with a gamma size distribution and wavelength-dependent, complex refractive indices following *Segelstein* [1981]. In order to deal with the strongly peaked phase functions of cloud particles, we use the correction of *Nakajima and Tanaka* [1988] in combination with 16 Gaussian streams to describe the diffuse intensity field. The retrieval algorithm can, optionally, retrieve the column-integrated number of cloud droplets and the fraction of cloud cover simultaneously with the aerosol and surface parameters. Other cloud parameters such as the size distribution, cloud top height, and geometrical thickness should be provided as auxiliary data and are assumed a priori in the retrieval. An overview of the fit parameters corresponding to the aerosol-only and the simultaneous aerosol-cloud retrieval is given in Table 2.

In this study, specifically, the effective radius of the cloud droplets assumed in the retrieval is taken from the median cloud droplet effective radii in the model grid cells in the column observed at nadir that contain liquid water. The effective variance of the size distribution is assumed to be $v_{\text{eff}}^{\text{cloud}} = 0.1$. The cloud top height is also taken from the model input as the height below which 95% of the liquid water resides. The cloud bottom is assumed fixed at 700 m. Note that this detail of information on the cloud is most likely not available for real observations. In the present study, however, we want to focus on 3-D effects and want to avoid cases where the retrieval does not converge because of incorrect assumptions on the clouds. Like in the synthetic measurements, the aerosol is homogeneously distributed between 0 and 700 m and a black surface has been used.

A detailed comparison of MYSTIC and the 1-D RT model employed by the inversion algorithm is performed by *Stap et al.* [2016]. The models are in good agreement for Rayleigh atmospheres, an atmosphere with Rayleigh and aerosol scattering as well as an atmosphere with a liquid water cloud layer above an aerosol layer. For more details the reader is referred to *Stap et al.* [2016].

3. Results

We present the synthetic observations in section 3.1. Geometrical 3-D effects as well as 3-D radiative effects and cloud contamination cause differences between the synthetic 3-D observations and 1-D RT simulations for an aerosol-only atmosphere. These effects are discussed in, respectively, sections 3.2 and 3.3. Two types of retrievals have been performed on the synthetic measurements: (i) the aerosol-only retrieval, where only the parameters of a bimodal aerosol distribution (i.e., no cloud mode) are fitted to the synthetic 3-D measurements, and (ii) the simultaneous aerosol and cloud retrieval, where both a bimodal aerosol distribution and the column-integrated number of cloud droplets and fraction of cloud cover are retrieved using the IPA

21698996, 2016, 21, Downloaded from https://agupubs.onlinelibrary.wiley.com/doi/10.1002/2016JD024787, Wiley Online Library on [24/02/2025]. See the Terms and Conditions (https://onlinelibrary.wiley.com/terms-and-conditions) on Wiley Online Library for rules of use; OA articles are governed by the applicable Creative Commons License

Table 3. The Number of Pixels per Resolution as Well as the Number of Pixels That Are Completely Cloud Free at All Angles, for Both Cloud Distributions

Cloud Distribution	Spatial Resolution	No. of Pixels	Cloud-Free Pixels
Case A	2×2 km^2	625	110
	4×4 km^2	144	10
	6×6 km^2	64	1
Case B	2×2 km^2	625	101
	4×4 km^2	144	11
	6×6 km^2	64	1

(see Table 2). The results of the aerosol-only retrieval are presented in section 3.4. In section 3.5 the results of the simultaneous aerosol and cloud retrieval are presented. Here we also discuss where the simultaneous aerosol and cloud retrieval can improve over aerosol-only retrievals.

3.1. Synthetic Observations

Figure 1 shows the simulated reflectances for the two cloud distributions and the fine absorbing aerosol case (type A). Shadows in the Rayleigh and aerosol signal can be seen northeast of larger clouds. The cloud distribution of case A has numerous small patches of clouds in the northwestern part of the domain. Observations in this region likely are cloud contaminated. The other three quadrants of the scene of case A contain large cloud formations. The reflectance image for case B shows larger-scale clouds. Cloud-free observations can be found east, west, and northwest of the center.

The 2×2 km^2 ground pixels of the synthetic observations that are completely cloud free at all angles are indicated in green in Figure 1. Table 3 lists the number of completely cloud free observations per ground pixel resolution for both cloud distributions. The fraction of cloud-free observations decreases from ~17% to 2% from the highest to the lowest satellite resolution.

3.2. Geometrical 3-D Effects

In Figure 1 there is a range of roughly 4 km to the north and south of cloudy pixels wherein no cloud-free observations are found. This is a result of the viewing geometry, where at higher VZA clouds above neighboring ground pixels are in the line of sight. In order to illustrate this, the reflectances of the models are shown at the first VZA ($\theta_{sat} = 63°$ and $\phi_{sat} = 180°$) and last VZA ($\theta_{sat} = 63°$ and $\phi_{sat} = 0°$) as well as the nadir observation of the domain in Figures 3 and 4. An example of a measurement that is affected by geometrical 3-D effects is shown in Figure 5.

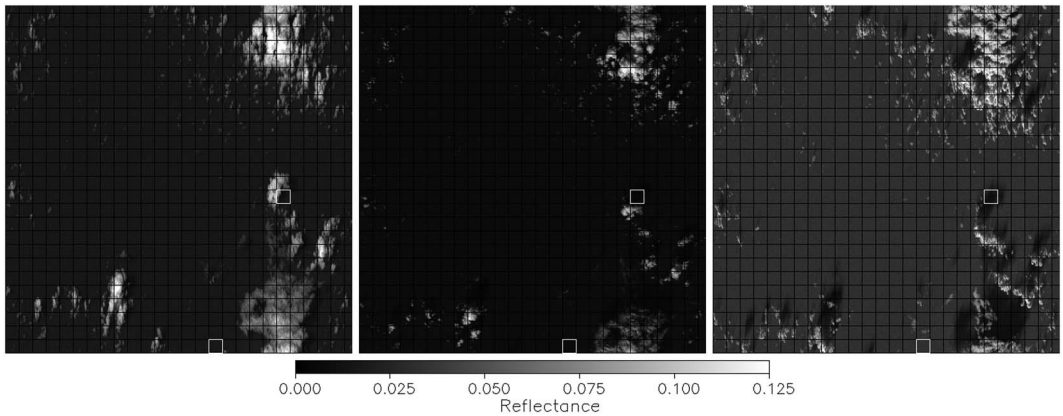

Figure 3. The satellite images for the reflectance at 670 nm at three different VZA for the cloud distribution of case A. A black grid indicates the 2×2 km^2 ground pixels. Two pixels are indicated with a white contour; for these, the simulated measurements are shown in Figure 5. (left) The satellite is in the south looking toward the north ($\theta_{sat} = 63°$ and $\phi_{sat} = 180°$). (middle) The satellite image at nadir ($\theta_{sat} = 0°$). (right) The satellite is in the north looking toward the south ($\theta_{sat} = 63°$ and $\phi_{sat} = 0°$).

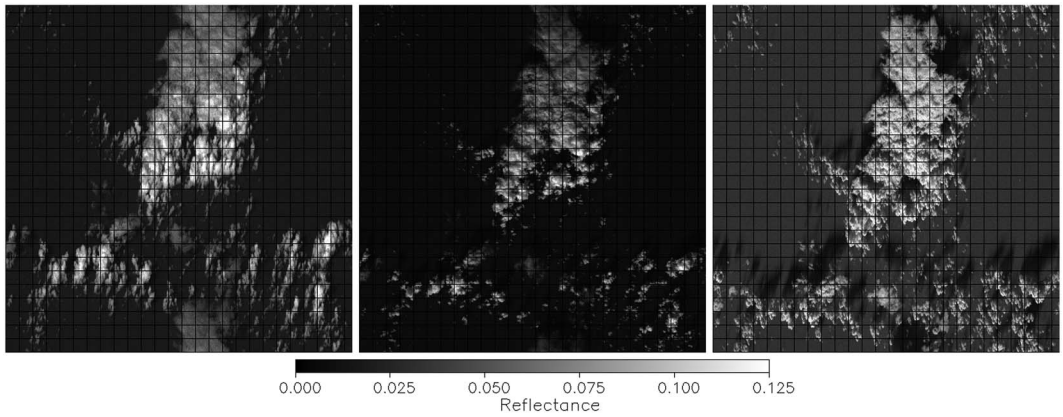

Figure 4. The satellite images for the reflectance at 670 nm at three different VZA for the cloud distribution of case B. A black grid indicates the 2×2 km^2 ground pixels. (left) The satellite is in the south looking toward the north ($\theta_{sat} = 63°$ and $\phi_{sat} = 180°$). (middle) The satellite image at nadir ($\theta_{sat} = 0°$). (right) The satellite is in the north looking toward the south ($\theta_{sat} = 63°$ and $\phi_{sat} = 0°$).

3.3. Cloud Contamination and 3-D Effects in the Synthetic Observations

In order to analyze how strong the clouds influence the cloud-free and nearly cloud free synthetic observations, via 3-D radiative effects and due to cloud contamination, the synthetic measurements created with MYSTIC are compared to a 1-D RT model that includes correct scattering and absorption by air molecules and aerosols, but no clouds. This model will be referred to as the aerosol-only model. The difference between the two is quantified by calculating a χ^2 (see equation (6)) with synthetic measurements created with MYSTIC and the 1-D RT model taken as, respectively, the measurement and model vector, with an assumed measurement uncertainty for the generic instrument of 0.5% on the intensity and 0.0035 absolute on the DoLP. In order to visualize where and how strong the influence of the clouds on the synthetic observations is, the χ^2 values are shown on the reflectance maps for four examples in Figures 6 and 7.

In Figure 6 (left) there are numerous pixels with $\chi^2 < 1.0$ indicating that (for this case) the assumed measurement noise is larger than the actual differences between the MYSTIC and the 1-D aerosol calculations. When this figure is compared with Figure 1, it is clear that as can be expected, most measurements with $\chi^2 < 1.0$ are found for measurements that are completely cloud free at all angles. Note that there are also pixels that are not completely cloud free at all angles (i.e., cloud contaminated) which still have $\chi^2 < 1.0$. The cloud contamination in these cases is small, usually less than 1% at a few angles. On the other hand, there are pixels that

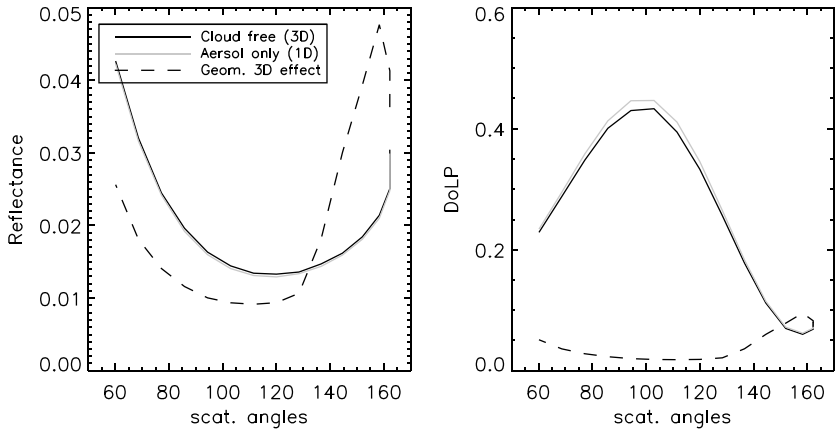

Figure 5. Example of an observation that is completely cloud free at all angles, an observation that is affected by geometrical 3-D effects and a (1-D) aerosol-only model. For all cases the measurement in the 490 nm band is shown for the scene with the case A cloud distribution, the fine absorbing aerosol, and SZA = 60°. The ground pixels of the cloud-free and geometrical 3-D effect cases are highlighted in Figure 3 on, respectively, the 16th column and 25th row and 21st column and 14th row. The measurements at 162°, 120°, and 60° scattering angle correspond to Figure 3 (right, middle, and left).

21698996, 2016, 21, Downloaded from https://agupubs.onlinelibrary.wiley.com/doi/10.1002/2016JD024787, Wiley Online Library on [24/02/2025]. See the Terms and Conditions (https://onlinelibrary.wiley.com/terms-and-conditions) on Wiley Online Library for rules of use; OA articles are governed by the applicable Creative Commons License

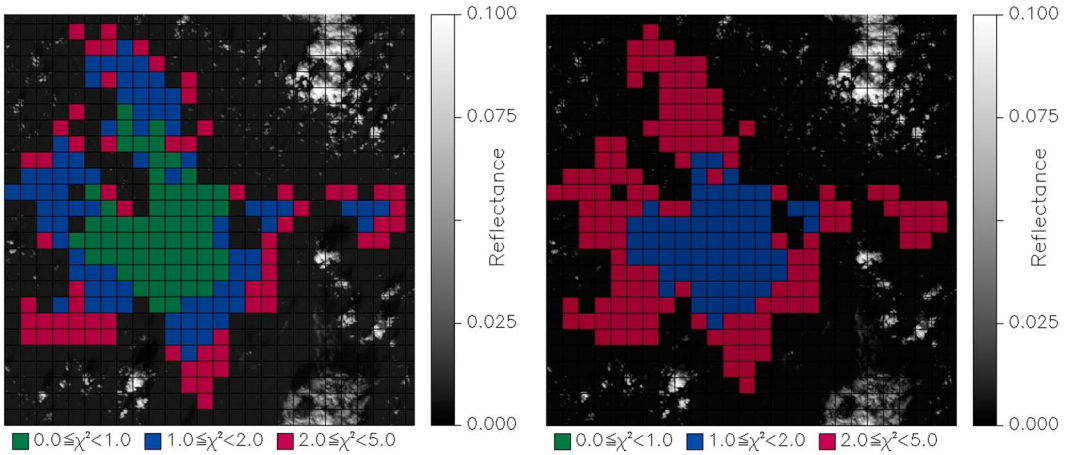

Figure 6. The quality of the (1-D) aerosol-only approximation to the synthetic measurements from the 3-D calculation in terms of the χ^2 difference between the 1-D forward model and the 3-D synthetic measurements, for the cloud distribution of case A, with SZA = 60°, (left) the fine absorbing aerosol and (right) the coarse nonspherical aerosol (type B) at 2×2 km^2 resolution.

are completely cloud free at all angles which do not have $\chi^2 < 1.0$. This is due to 3-D effects of the clouds (i.e., shadows and cloud-induced radiance enhancements). It should be noted that the 3-D effect of cloud-induced radiance enhancement depends on wavelength and is different for total radiance than for polarized radiance. Namely, this 3-D effect is strongest in blue because there, the Rayleigh scattering optical thickness is largest, resulting in an increased chance that a photon is scattered by a cloud droplet and an air molecule. Also, the 3-D radiance enhancement is much weaker in polarized radiance than in total radiance, because polarized radiance mostly originates from photons that have been scattered only once or twice. These considerations only hold for the 3-D radiance enhancement. The geometric 3-D effects are comparable for the different wavelength and between total radiance and polarized radiance.

The reflectance of the 3-D model is systematically higher, and related to that, the DoLP is systematically lower than reflectance and DoLP of a (1-D) aerosol-only calculation. An example of this is shown in Figure 5. This systematic offset is found everywhere in the domain, even for the measurements that are farthest away from the clouds. Cloud-induced radiance enhancements are the cause for the increased reflectance relatively far away from clouds. As expected, these systematic differences become larger (increasing the χ^2 values) with decreasing distance to the clouds.

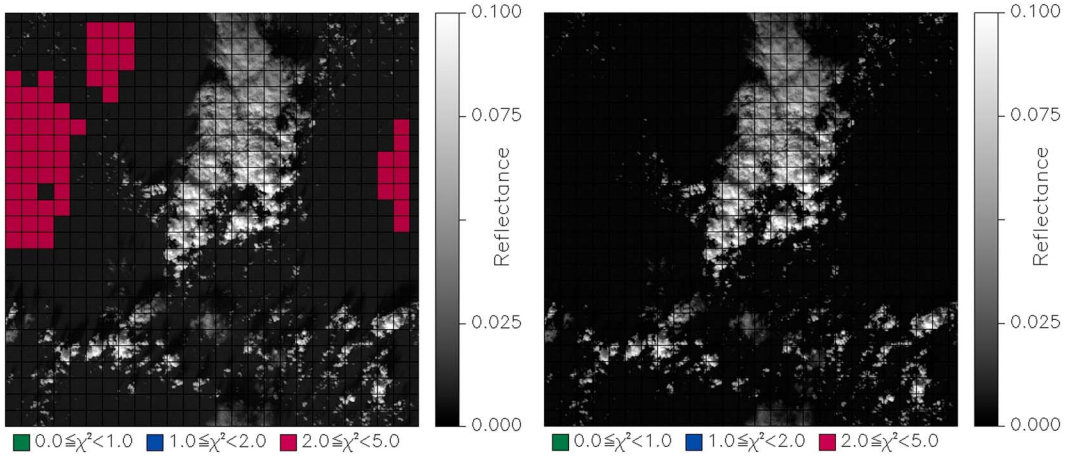

Figure 7. The quality of the (1-D) aerosol-only approximation to the synthetic measurements from the 3-D calculation in terms of the χ^2 difference between the 1-D forward model and the 3-D synthetic measurements, for the cloud distribution of case B, with SZA = 60°, (left) the fine absorbing aerosol and (right) the coarse nonspherical aerosol (type B) at 2×2 km^2 resolution.

21698996, 2016, 21, Downloaded from https://agupubs.onlinelibrary.wiley.com/doi/10.1002/2016JD024787, Wiley Online Library on [24/02/2025]. See the Terms and Conditions (https://onlinelibrary.wiley.com/terms-and-conditions) on Wiley Online Library for rules of use; OA articles are governed by the applicable Creative Commons License

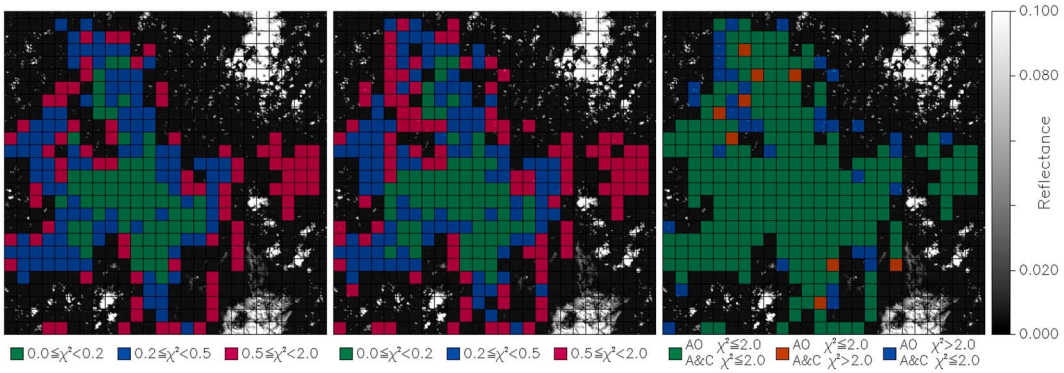

Figure 8. (left and middle) The goodness of fit obtained in, respectively, the aerosol-only and simultaneous aerosol and cloud retrievals as a χ^2 value at 2×2 km^2 satellite resolution for the cloud distribution of case A with SZA = 40° and the coarse nonspherical aerosol. (right) Where and which retrieval obtained a good enough fit ($\chi^2 \leq 2.0$). Here "AO" stands for aerosol-only retrieval and "A&C" stands for simultaneous aerosol and cloud retrieval.

For the coarse nonspherical case (type B), with lower AOT, the aerosol signal is smaller; thus, cloud contamination and 3-D radiative effects have a relatively large effect on the measurements (see Figure 6, right). As a result there are no pixels with $\chi^2 < 1.0$. The same trend toward increased χ^2 at closer vicinity to the clouds is found.

The 3-D effects are even more important in the synthetic measurements from the scenes with cloud distribution of case B (see Figure 7). Here the χ^2 values of the measurements, when compared with the aerosol-only model, are rarely lower than 5.0. Note that case B has roughly 3 times more condensed water than case A.

3.4. Aerosol-Only Retrievals

The standard aerosol-only retrievals have been performed on all the synthetic measurements. In the normal setup of the algorithm the first guess of the fit parameters is obtained using a look-up table-based retrieval or, alternatively, by a neural network retrieval (as in the work by *Di Noia et al.* [2015]). In the present study we focus on 3-D effects and want to avoid cases where the retrieval does not converge because the first guess deviates too much from the truth. Therefore, for the synthetic retrievals of this paper we use the truth as first guess. It should be noted that we can achieved virtually the same results if we perform five independent retrievals using the best fitting models of the LUT as first guess. This has been verified for selected cases, but for reasons of computational effort we do not further use this approach in this paper. Following *Stap et al.* [2015], a goodness-of-fit criterion is applied as a filter for cloud contamination. Only retrievals for which the fit to the measurement has $\chi^2 \leq 2.0$ are used in the analysis. The measurement uncertainty is assumed to be 0.5% on the intensity and 0.0035 absolute on the DoLP for the generic instrument considered here.

Figures 8 (left) and 9 (left) show for two examples the spatial distribution of the quality of the fit to the synthetic MYSTIC measurement that is obtained by the retrieval algorithm. As expected, the best fits (i.e., lowest χ^2 values) are obtained farthest away from clouds. In the scenes with more clouds and lower aerosol loads, where the 3-D RT effects are strongest, the quality of the fits is lower.

In 99, 98, and 100% of the measurements that are completely cloud free at all angles, a fit with $\chi^2 \leq 2.0$ is obtained for, respectively, 2×2, 4×4, and 6×6 km^2 resolution. The few cases where the retrieval algorithm did not obtain a good fit to a cloud-free measurement are only found in the scenes with cloud distribution of case B and mostly occur for the coarse nonspherical case (type B) which has low AOT. In these scenes the 3-D radiative effects are strongest (see section 3.3). For these measurements the goodness-of-fit filter successfully filters for 3-D radiative effects. The goodness of fit after the retrieval is, in general, better than before the retrieval (Figure 6), which means that to a certain extent the 3-D radiative effects are fit by erroneous adjustments to the bimodal aerosol model. Below we will investigate to what extent the aerosol parameters are affected by this compensation for the 3-D effects.

At 2×2 km^2 resolution 88% of the observations with cloud fractions below 5% obtained a fit with $\chi^2 \leq 2.0$. For 4×4 and 6×6 km^2 resolutions these numbers are 97% and 90%, respectively. In only 3% of the measurements with cloud fractions >5% a fit with $\chi^2 \leq 2.0$ is obtained (same for all spatial resolutions). This shows that measurements which have more than 5% cloud cover at one or more angles are filtered very efficiently by a

21698996, 2016, 21, Downloaded from https://agupubs.onlinelibrary.wiley.com/doi/10.1002/2016JD024787, Wiley Online Library on [24/02/2025]. See the Terms and Conditions (https://onlinelibrary.wiley.com/terms-and-conditions) on Wiley Online Library for rules of use; OA articles are governed by the applicable Creative Commons License

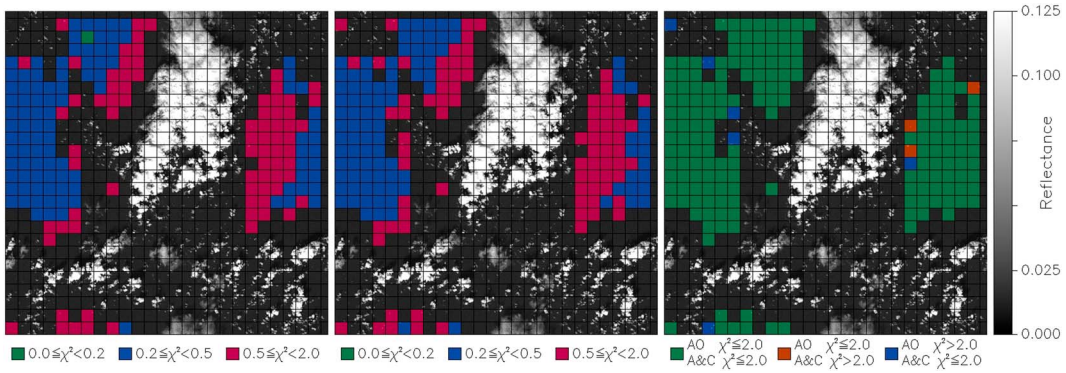

Figure 9. The same as Figure 8 but for the cloud distribution of case B, with SZA = 40° and the fine absorbing aerosol.

posteriori goodness-of-fit criterion. This is in line with the findings of aerosol-only retrievals in real PARASOL observations of *Stap et al.* [2015]. Smaller amounts of cloud contamination are difficult to filter by the goodness-of-fit criterion. Below we show that these very low amounts of cloud contamination only have a small effect on the correct retrieval of the aerosol parameters.

In Table 4 the bias in the retrieved aerosol parameters is listed per aerosol case for 2×2 km^2 resolutions. The statistics found at the other two resolutions are not significantly different and are therefore not shown. The quality of the retrieved aerosol parameters is checked against the accuracy requirements for aerosol properties in light of climate research as formulated by *Mishchenko et al.* [2004] for the Aerosol Polarimetry Sensor: 0.02 or 7% for the AOT for over ocean scenes, 0.03 on the SSA, 0.02 on the m_r, and 0.1 μm on r_{eff} for each mode.

There is a tendency toward underestimated total AOT in the fine absorbing aerosol cases (type A) with a bias of −0.010 (−1.3%), which is within the requirements in the overall set of observations with this aerosol type. For the scene with the fine absorbing aerosol (type A), cloud distribution of case B and SZA = 40° the bias in the retrieved total AOT is −0.037 (or −4.6%) with a standard deviation of 0.014. There are no significant differences in the retrieved AOTs at the other spatial resolutions.

There is a systematic overestimate of the SSA in all scenes. The bias in SSA is outside the accuracy requirements for three out of eight scenes (see Table 5). As expected, the overestimate is largest in scenes with stronger 3-D effects; those with the cloud distribution of case B and the scenes with the lower aerosol load (i.e., the coarse nonspherical aerosol case, type B).

Table 4. The Bias and, Between Parentheses, Standard Deviation for a Selection of the Aerosol Parameters Retrieved With the Aerosol-Only Algorithm for the Retrievals at 2×2 km^2 Resolution (at Both SZA and Cloud Distribution of Both Cases A and B)[a]

Variable	Fine Absorbing	Coarse Nonspherical
n	903	832
$\tau^f_{550\,nm}$	−0.015 (0.015)	0.001 (0.004)
$\tau^c_{550\,nm}$	0.005 (0.009)	0.001 (0.007)
$SSA_{670\,nm}$	0.020 (0.013)	0.035 (0.017)
r^f_{eff} (μm)	−0.00 (0.00)	−0.01 (0.00)
m^f_r	0.004 (0.008)	0.107 (0.040)
r^c_{eff} (μm)	−0.02 (0.31)	−0.01 (0.06)
m^c_r	−0.005 (0.012)	0.002 (0.010)
Sph^c	−0.124 (0.106)	−0.010 (0.010)

[a]Superscript f and c denote fine mode and coarse mode. The statistics are separated by aerosol case.

21698996, 2016, 21, Downloaded from https://agupubs.onlinelibrary.wiley.com/doi/10.1002/2016JD024787, Wiley Online Library on [24/02/2025]. See the Terms and Conditions (https://onlinelibrary.wiley.com/terms-and-conditions) on Wiley Online Library for rules of use; OA articles are governed by the applicable Creative Commons License

Table 5. The Bias and, Between Parentheses, Standard Deviation of the Retrieved SSA for the Retrievals Performed With the Aerosol-Only Algorithm on the Synthetic Measurements at 2×2 km^2 Resolution

Cloud distribution	SZA	Aerosol Case	$SSA_{670\,nm}$
Case A	40°	fine absorbing	0.019 (0.007)
Case A	40°	coarse nonspherical	0.026 (0.010)
Case A	60°	fine absorbing	0.009 (0.005)
Case A	60°	coarse nonspherical	0.022 (0.011)
Case B	40°	fine absorbing	0.041 (0.010)
Case B	40°	coarse nonspherical	0.055 (0.007)
Case B	60°	fine absorbing	0.017 (0.006)
Case B	60°	coarse nonspherical	0.051 (0.011)

Apparently, the retrieval algorithm compensates for the enhancement in radiation due to the 3-D radiative effect by a too high SSA (i.e., more scattering) for both aerosol cases.

The retrieved effective radii of both aerosol modes are well within required accuracy. While the real refractive index of the fine mode is retrieved well for the fine absorbing aerosol case (type A), it is largely overestimated in the coarse nonspherical aerosol case (type B). Note, however, that the coarse nonspherical aerosol case (type B) only has a small amount of fine mode aerosol (see Table 1), which leads to a low sensitivity to the microphysical parameters of this aerosol mode.

There is an underestimate in the retrieved sphericity of the fine absorbing aerosol (type A). Note that this aerosol case is dominated by the fine mode which results in a low sensitivity to this coarse mode parameter. In the coarse nonspherical case (type B), where the coarse mode aerosol and its sphericity play an important role, this parameter is retrieved with high accuracy.

We have taken a closer look at the retrieved aerosol parameters with respect to the presence of cloud contamination and vicinity to clouds. One might, for example, expect higher values for the retrieved AOT in cloud-contaminated observations. This is indeed found in the data. Especially for the fine mode absorbing aerosol (type A), this effect competes with the trend toward underestimated AOT which is caused by 3-D radiative effects. In the overall data set, at 2×2 km^2 resolution, the retrieval error in the total AOT is −0.007 for the cloud-free scenes, −0.003 for the scenes with $f \leq 5\%$ (at one or more angles), and 0.006 for the clouded cases with $f \geq 5\%$ (at one or more angles). The trend toward higher AOT in cloud-contaminated observations is more pronounced at lower spatial resolution. At 6×6 km^2 resolution the retrieval error in total AOT is −0.008 for the cloud-free scenes, −0.001 for the scenes with small amounts of cloud contamination, and 0.015 for the clouded cases. For the SSA a trend toward smaller bias in the clouded scenes is found. The retrieval error in the SSA is 0.030 for the cloud-free scenes, 0.025 for the scenes with small amounts of cloud contamination, and 0.022 for the clouded cases. Unlike the retrieved AOT, the trend in the bias of the SSA is not different at the other spatial resolutions. In the retrieved microphysical aerosol parameters no trends in the retrieval bias are found with respect to cloud contamination. Recall that relatively few clouded cases pass the goodness-of-fit criterion and thus the differences in the retrieval biases due to cloud contamination, found for the AOT and SSA, have almost no effect on the retrieval statistics of the overall data set.

Figure 10 shows the spatial pattern of the AOT and SSA errors for the fine absorbing aerosol case (type A) for SZA = 40° and 60° at 6×6 km^2 resolution. Some pixels where a retrieval with $\chi^2 \leq 2.0$ is achieved contain small clouds, and this generally results in a small overestimate of AOT. This is expected as the higher aerosol load compensates for the higher reflectances that are caused by the clouds. At SZA = 40°, the measurements that do not visibly have any cloud contamination often have an underestimated AOT. The higher reflectances (caused by 3-D radiative effects) and resulting lower DoLP, compared to the 1-D aerosol-only model here, are compensated by lowering the absorptivity of the aerosol, which translates into a higher SSA (see Figure 10, bottom row). While one might expect a relation between the degree of underestimation of AOT and overestimation of SSA, this is not found in the data. At SZA = 60° (Figure 10, left column) the 3-D radiative effects are of smaller influence. Compared to the measurements at SZA = 40°, there are smaller retrieval errors for both AOT and SSA.

21698996, 2016, 21, Downloaded from https://agupubs.onlinelibrary.wiley.com/doi/10.1002/2016JD024787, Wiley Online Library on [24/02/2025]. See the Terms and Conditions (https://onlinelibrary.wiley.com/terms-and-conditions) on Wiley Online Library for rules of use; OA articles are governed by the applicable Creative Commons License

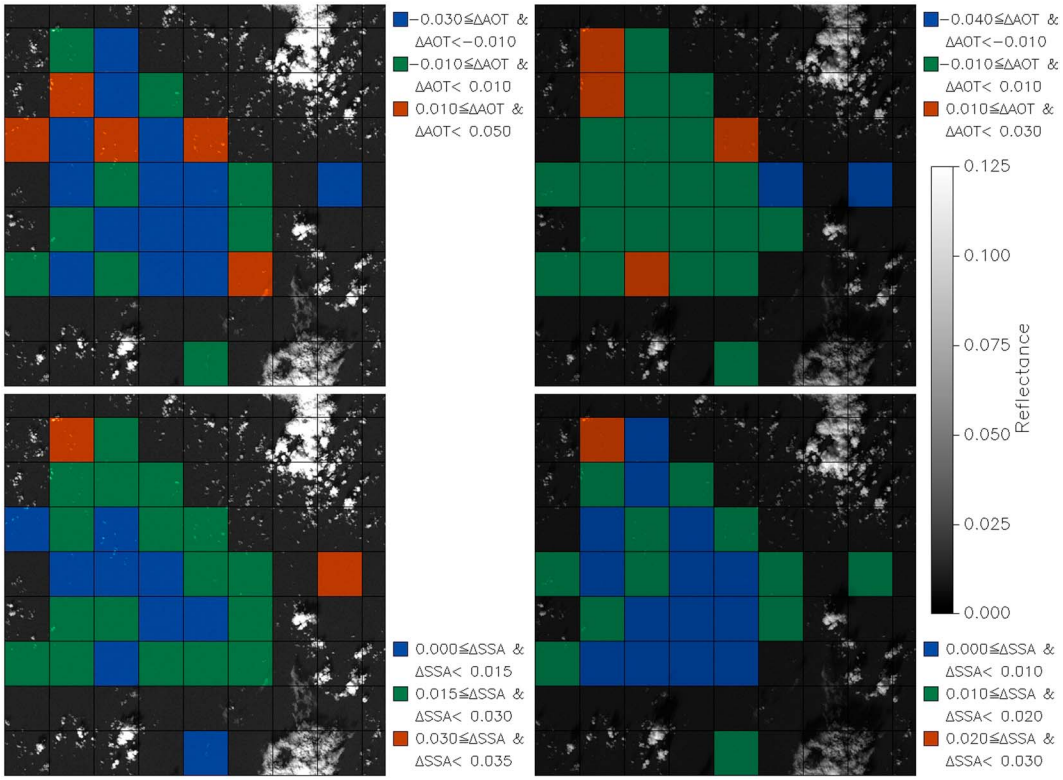

Figure 10. The bias in the retrieved total (top row) AOT and (bottom row) SSA for the aerosol-only retrievals with $\chi^2 \leq 2.0$ in the scene with cloud distribution of case A, the fine absorbing aerosol, and (left column) SZA = 40° and (right column) SZA = 60°.

3.5. Simultaneous Aerosol and Cloud Retrievals

In this section we will investigate whether the aerosol retrievals in the vicinity of clouds and for pixels with (small) cloud contamination, as discussed above, can be improved by performing a simultaneous aerosol cloud retrieval.

Simultaneous aerosol and cloud retrievals have been performed on all the synthetic MYSTIC measurements. Similar to the aerosol-only retrievals, for the first guess state vector the true aerosol parameters are used. For cloud parameters in the first guess state vector the median of the COT and median effective radius of all model columns at nadir that contain any liquid water are used. For the coverage fraction the fraction of model columns at nadir that contain any liquid water is used as first guess. When no cloud is present at nadir, $\tau^{\text{cloud}}_{550\,\text{nm}} = 1.0$, $r^{\text{cloud}}_{\text{eff}} = 8.0\,\mu\text{m}$, and $f = 0.0$ are assumed as first guess. As with the aerosol-only retrievals, retrievals that do not result in a fit with $\chi^2 \leq 2.0$ are not used in the analysis.

3.5.1. Goodness of Fit

Figures 8 (middle) and 9 (middle) give two examples that indicate the quality of the fit to the synthetic measurement that is obtained. Like the aerosol-only retrievals, the simultaneous aerosol and cloud retrieval shows a trend toward higher-quality fits at larger distances from clouds and an overall better quality of fits in scenes with smaller 3-D RT effects.

In 95, 94, and 100% of the measurements that are completely cloud free at all angles a fit with $\chi^2 \leq 2.0$ is obtained for, respectively, 2×2, 4×4, and 6×6 km^2 resolution. Similar to what was found with the aerosol-only retrievals, the synthetic measurements from the scenes with the strongest 3-D RT effects (case B with the low load of coarse nonspherical aerosol, type B) are more difficult to fit. Thus, adjustments to the aerosol and/or cloud parameters in the state vector compensate for the 3-D radiative effects in the measurements to a certain extent, but do not fully reproduce them.

At 2×2 km^2 resolution a fit with $\chi^2 \leq 2.0$ is obtained in 92% of the cases with cloud fractions below 5%. At 4×4 and 6×6 km^2 resolutions these numbers are 98% and 93%, respectively. In only 6% of the measurements with $f \geq 5\%$ (at one or more angles) a fit with $\chi^2 \leq 2.0$ is obtained (at 2×2 km^2 resolution). At 4×4 and 6×6 km^2

21698996, 2016, 21, Downloaded from https://agupubs.onlinelibrary.wiley.com/doi/10.1002/2016JD024787, Wiley Online Library on [24/02/2025]. See the Terms and Conditions (https://onlinelibrary.wiley.com/terms-and-conditions) on Wiley Online Library for rules of use; OA articles are governed by the applicable Creative Commons License

Table 6. The Bias and, Between Parentheses, Standard Deviation of the Retrieved Aerosol Parameters for the Retrievals Performed With the Simultaneous Aerosol and Cloud Algorithm on the Synthetic Measurements at 2×2 km^2 Resolution, at Both SZA and Cloud Distribution of Both Cases A and B

Variable	Fine Absorbing	Coarse Nonspherical
n	932	881
$\tau^{f}_{550\,nm}$	−0.014 (0.015)	0.002 (0.004)
$\tau^{c}_{550\,nm}$	0.003 (0.008)	−0.002 (0.007)
$SSA_{670\,nm}$	0.019 (0.013)	0.037 (0.018)
r^{f}_{eff} (μm)	0.00 (0.00)	−0.01 (0.00)
m^{f}_{r}	0.003 (0.007)	0.103 (0.046)
r^{c}_{eff} (μm)	0.04 (0.21)	−0.02 (0.07)
m^{c}_{r}	−0.003 (0.012)	0.005 (0.009)
Sph^{c}	−0.078 (0.077)	−0.008 (0.009)

resolutions these numbers are 10% and 13%. Only a fraction of the partially clouded measurements can be reproduced with the simultaneous aerosol and cloud algorithm. This is understandable since the IPA (which has one cloud fraction at all angles) ignores geometrical 3-D and 3-D radiative effects.

3.5.2. Retrieved Aerosol Properties

In Table 6 the bias in the retrieved aerosol parameters is listed per aerosol case for 2×2 km^2 resolutions. The retrieved total AOT in the overall data set is within the requirements. In the scene with the cloud distribution of case B, SZA = 40° and the fine absorbing aerosol (type A) the total AOT is systematically underestimated by 0.036 (or 4.5%) with a standard deviation of 0.015. There are no significant differences in the retrieved AOTs at different satellite resolutions. The accuracy with which the effective radii of both modes, the real part of the refractive index of both modes, and the sphericity of the coarse mode are retrieved is nearly identical to what is found with the aerosol-only retrieval. The SSA is systematically overestimated and is outside of the accuracy requirements in four out of eight scenes (see Table 7). This is similar to what is found with the aerosol-only retrieval.

One could expect simultaneous aerosol and cloud retrieval to be an improvement over the aerosol-only retrieval in cloud-contaminated or partially clouded observations, as it is better suited to account for the signal of the clouds. In Figures 8 (right) and 9 (right) it is indicated where both retrievals are able to obtain a good fit, where the simultaneous aerosol and cloud retrieval works while the aerosol-only does not and vice versa. Here green indicates an equal quality of fit in both retrievals, blue is used to indicate pixels where the simultaneous aerosol and cloud retrieval outperforms the aerosol-only retrieval, and orange highlights the pixels where the aerosol-only retrieval works while the simultaneous aerosol and cloud retrieval does not. At 2×2 km^2 resolution there are a few pixels where the simultaneous aerosol and cloud retrieval outperforms

Table 7. The Bias and, Between Parentheses, Standard Deviation of the Retrieved SSA for the Retrievals Performed With the Simultaneous Aerosol and Cloud Algorithm on the Synthetic Measurements at 2×2 km^2 Resolution, Separated by Cloud Distribution, SZA, and Aerosol Type

Cloud Distribution	SZA	Aerosol Case	$SSA_{670\,nm}$
Case A	40°	fine absorbing	0.019 (0.007)
Case A	40°	coarse nonspherical	0.030 (0.011)
Case A	60°	fine absorbing	0.008 (0.006)
Case A	60°	coarse nonspherical	0.026 (0.015)
Case B	40°	fine absorbing	0.040 (0.010)
Case B	40°	coarse nonspherical	0.058 (0.006)
Case B	60°	fine absorbing	0.017 (0.006)
Case B	60°	coarse nonspherical	0.052 (0.012)

21698996, 2016, 21, Downloaded from https://agupubs.onlinelibrary.wiley.com/doi/10.1002/2016JD024787, Wiley Online Library on [24/02/2025]. See the Terms and Conditions (https://onlinelibrary.wiley.com/terms-and-conditions) on Wiley Online Library for rules of use; OA articles are governed by the applicable Creative Commons License

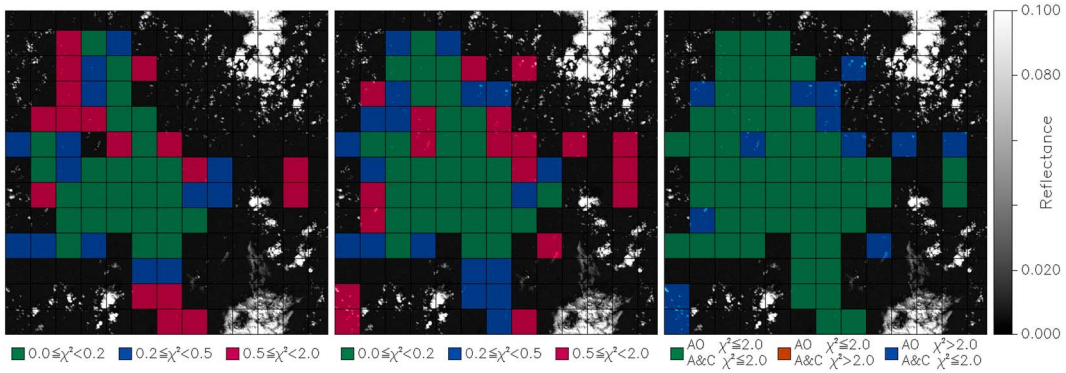

Figure 11. The same as Figure 8 but at 4×4 km^2 resolution.

the aerosol-only retrieval. At 4×4 and 6×6 km^2 resolutions the simultaneous aerosol and cloud outperforms the aerosol-only retrieval in more cases; see, for example, Figures 11 and 12. At these lower satellite resolutions the geometrical 3-D effects are less important (i.e., the cloud fractions are more likely to be similar at different VZA) and the simultaneous aerosol and cloud retrieval (with 1-D RT) is more successful at fitting the partial cloud cover. At 6×6 km^2 resolution it can be seen that indeed, the algorithm for simultaneous aerosol and cloud retrieval is able to fit measurements close to clouds that cannot be fitted using an aerosol-only retrieval. The partially clouded scenes where the simultaneous aerosol and cloud retrieval is able to reproduce the synthetic measurement mostly resemble broken cloud fields.

Table 8 divides the bias in AOT between, respectively, cloud-free cases, "cloud-contaminated" cases ($f \leq 5\%$), and "clouded" cases ($f \leq 5\%$). This is done for the three different spatial resolutions and for both the aerosol-only and aerosol-cloud retrievals. If we compare the aerosol-only with the aerosol-cloud retrievals, it can be seen that the aerosol-only retrievals show a clear trend in AOT bias going from "cloud free" to cloud contaminated to clouded, while this trend is much less pronounced for the aerosol-cloud retrievals. Especially when going from cloud free to cloud contaminated, there is virtually no trend for the aerosol-cloud retrievals. This is an important advantage over aerosol-only retrievals when one wants to study aerosol-cloud relationships. The improvement of aerosol-cloud retrievals over aerosol-only retrievals is most pronounced for the coarsest spatial resolution (6×6 km^2), because there, the goodness-of-fit filter for cloud contaminations is less effective than for higher spatial resolutions (see above). Furthermore, compared to the aerosol-only retrieval, there are more retrievals with $\chi^2 \leq 2.0$ for the aerosol-cloud retrievals (see Figure 10). These are measurements that have partial cloud cover in the form of a broken cloud field. Looking at the overall statistics (i.e., all cases together), there are no significant differences between the aerosol-only and the aerosol-cloud retrieval for the bias on the different aerosol parameters, because the overall statistics are dominated by cloud-free scenes where the two approaches show the same performance.

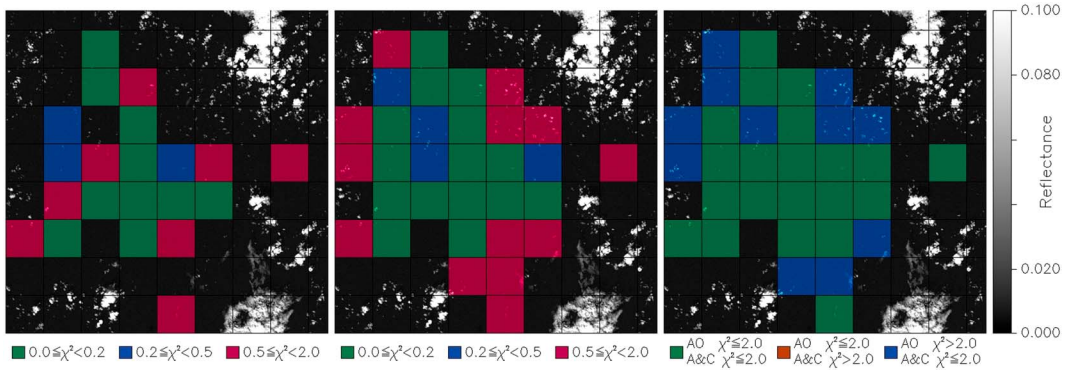

Figure 12. The same as Figure 8 but at 6×6 km^2 resolution.

21698996, 2016, 21, Downloaded from https://agupubs.onlinelibrary.wiley.com/doi/10.1002/2016JD024787, Wiley Online Library on [24/02/2025]. See the Terms and Conditions (https://onlinelibrary.wiley.com/terms-and-conditions) on Wiley Online Library for rules of use; OA articles are governed by the applicable Creative Commons License

Table 8. The Bias in AOT as a Function of Cloud Contamination[a]

Retrieval	Spatial Resolution	Cloud Free	Cloud Contaminated	Clouded
Aerosol only	2×2 km^2	−0.007	−0.003	0.006
Aerosol only	4×4 km^2	−0.008	−0.001	0.011
Aerosol only	6×6 km^2	−0.008	−0.001	0.015
Aerosol and cloud	2×2 km^2	−0.007	−0.006	−0.003
Aerosol and cloud	4×4 km^2	−0.008	−0.006	0.000
Aerosol and cloud	6×6 km^2	−0.008	−0.006	0.004

[a]Column 1 indicates whether the result was obtained with the aerosol-only retrieval or the simultaneous aerosol and cloud retrieval, and column 2 mentions the satellite resolution. Columns 3 to 5 list the mean retrieval error in AOT for the observations that, respectively, are completely cloud free at all angles, have small amounts of cloud contamination ($0\% < f \leq 5\%$ at one or more angles), and are partially clouded ($f \geq 5\%$ at one or more angles). The results contain the retrievals for the fine absorbing and coarse nonspherical aerosol types (types A and B) at both SZAs and both cloud distributions.

Figure 13 shows the spatial pattern of the AOT and SSA errors for the fine absorbing aerosol (type A) case for SZA = 40° and 60° at 6×6 km^2 resolution. Similar to what was found in the aerosol-only retrievals, AOT overestimates are found in measurements that have cloud contamination and AOT underestimates are mostly found in scenes that have less cloud contamination but are more likely to be influenced by 3-D radiative effects. Overall, the retrieved AOT corresponds well to the true AOT; in the scenes with fine absorbing aerosol (type A) the bias in the retrieved total AOT is −0.009 (−1.1%) with a standard deviation of 0.026. The SSA is, in general, slightly overestimated to compensate for the higher reflectances caused by 3-D effects.

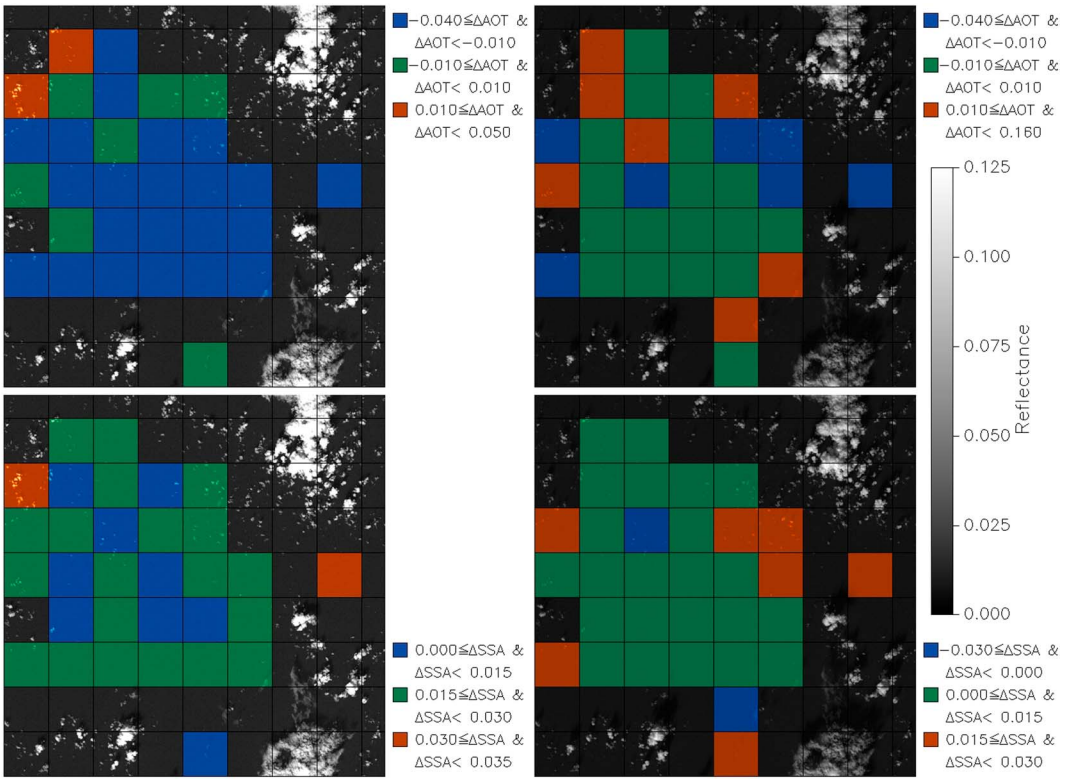

Figure 13. The bias in the retrieved total (top row) AOT and (bottom row) SSA for the simultaneous aerosol and cloud retrievals with $\chi^2 \leq 2.0$ in the scene with cloud distribution of case A, the fine absorbing aerosol (type A), and (left column) SZA = 40° and (right column) SZA = 60°.

21698996, 2016, 21, Downloaded from https://agupubs.onlinelibrary.wiley.com/doi/10.1002/2016JD024787, Wiley Online Library on [24/02/2025]. See the Terms and Conditions (https://onlinelibrary.wiley.com/terms-and-conditions) on Wiley Online Library for rules of use; OA articles are governed by the applicable Creative Commons License

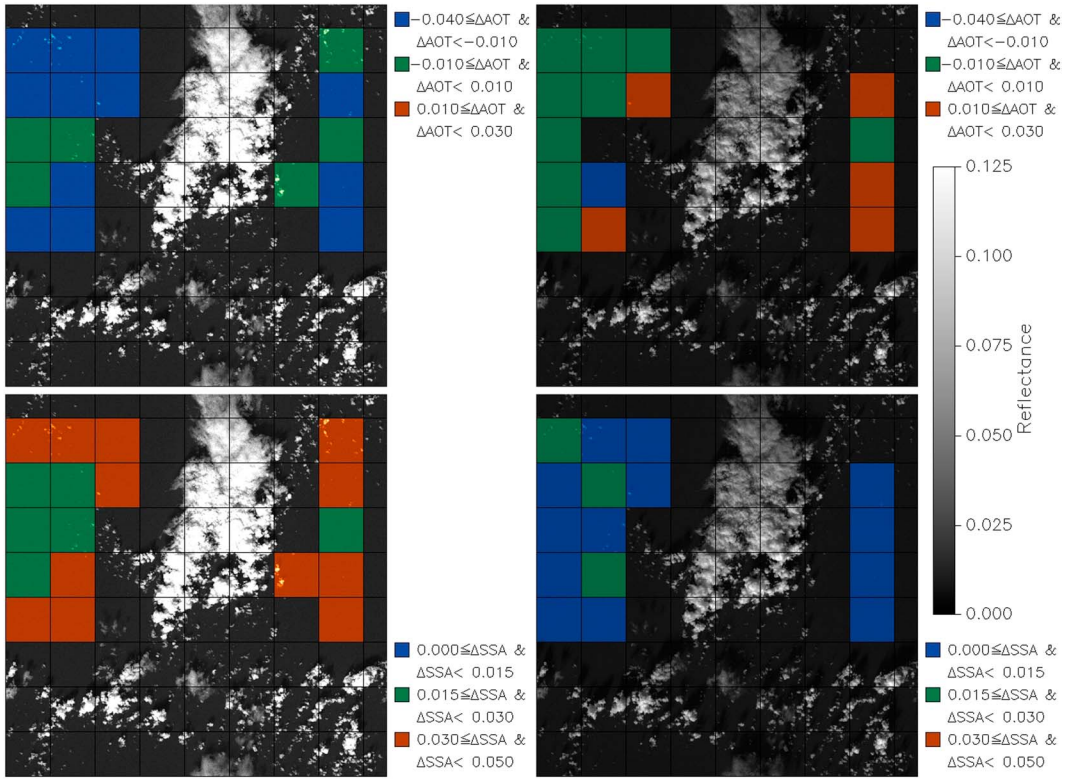

Figure 14. The same as Figure 13 but for the cloud distribution of case B.

Figure 14 shows the spatial pattern of the AOT and SSA errors like in Figure 13 but now for cloud case B. The general patterns are the same as for cloud case A, with larger errors for SZA = 40° than for 60° and an underestimate of the AOT combined with an overestimate of the SSA. However, the biases caused by 3-D cloud-induced radiance enhancements are larger for case B than for case A, because the 3-D effects are stronger for case B (see Figure 7). The negative bias in AOT can get as large as 0.04, and the positive bias in SSA can get as large as 0.05.

Overall, the errors on aerosol parameters caused by 3-D radiative transfer effects found in this study are smaller than those found by *Stap et al.* [2016] for generic scenes with simple cuboid clouds. However, the study of *Stap et al.* [2016] only considered cloud-contaminated cases with cloud fractions up to 20%, while the present study also includes cloud-free scenes in the vicinity of clouds. If we consider only cloud-contaminated scenes, our study shows errors on aerosol properties that are similar to those for the random cloud distributions of *Stap et al.* [2016] with a cloud fraction of 10%. Scenes at cloud edges are effectively screened out by our goodness-of-fit filter.

Figure 15 shows the retrieved cloud fraction for the simultaneous aerosol-cloud retrieval at 6×6 km^2 using the 1-D approximation versus the true cloud fraction used for the measurement simulation with MYSTIC. Here the true cloud fraction is defined as the ratio of the number of 50×50 m^2 grid boxes that are cloud contaminated and the total number of 50×50 m^2 grid boxes within a satellite pixel for a given spatial resolution. All cloud fractions larger than 0.15 are filtered out by the goodness-of-fit filter. Overall, the retrieved cloud fraction compares reasonably well with the true cloud fraction, but toward larger cloud fraction the 1-D retrieval tends to slightly underestimate the true cloud fraction. For some cases with very low cloud fraction (0.001) the 1-D retrieval yields a too high cloud fraction.

3.5.3. Effect of Spectral Range

As indicated above, the radiance enhancement in the surrounding of clouds because of 3-D effects becomes stronger at shorter wavelengths because of the higher Rahleigh optical thickness at these wavelengths [see, e.g., *Várnai and Marshak*, 2009]. Therefore, it seems plausible that 3-D-induced errors on aerosol parameters will be reduced if the 410 nm band is excluded from our retrievals. To investigate this, we performed the simultaneous aerosol cloud retrievals as shown in Figure 13 but leaving out the 410 nm band.

21698996, 2016, 21, Downloaded from https://agupubs.onlinelibrary.wiley.com/doi/10.1002/2016JD024787, Wiley Online Library on [24/02/2025]. See the Terms and Conditions (https://onlinelibrary.wiley.com/terms-and-conditions) on Wiley Online Library for rules of use; OA articles are governed by the applicable Creative Commons License

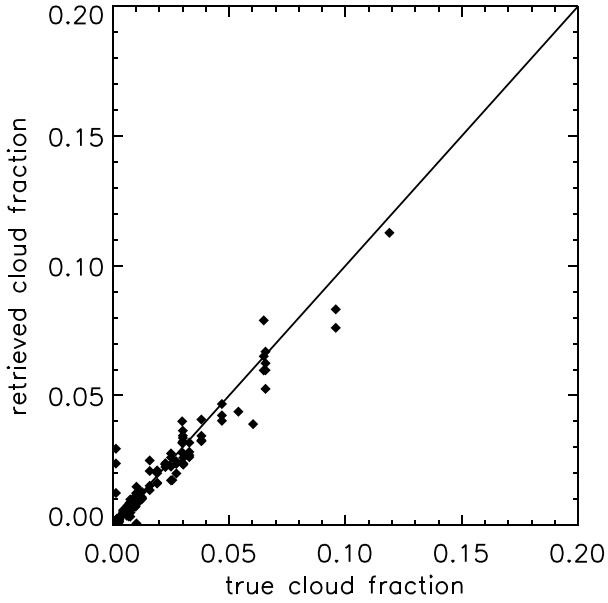

Figure 15. The retrieved versus the true, nadir cloud fraction in the simultaneous aerosols and cloud retrieval of the simulations of both the fine absorbing (type A) and coarse nonspherical (type B) aerosol types, at both SZA, for both cloud distributions at the 6 × 6 km^2 resolution. Here the true, nadir cloud fraction is calculated from the 3-D LWC input for MYSTIC.

The corresponding results are shown in Figure 16. If we compare Figures 13 and 16, it can be seen that indeed, the 3-D-induced errors on AOT and SSA errors are slightly reduced for retrievals that do not make use of the 410 nm band. This is in particular the case for regions where the 3-D radiance enhancements dominate over 3-D geometrical effects. For the corresponding pixels the AOT underestimation and SSA overestimation are

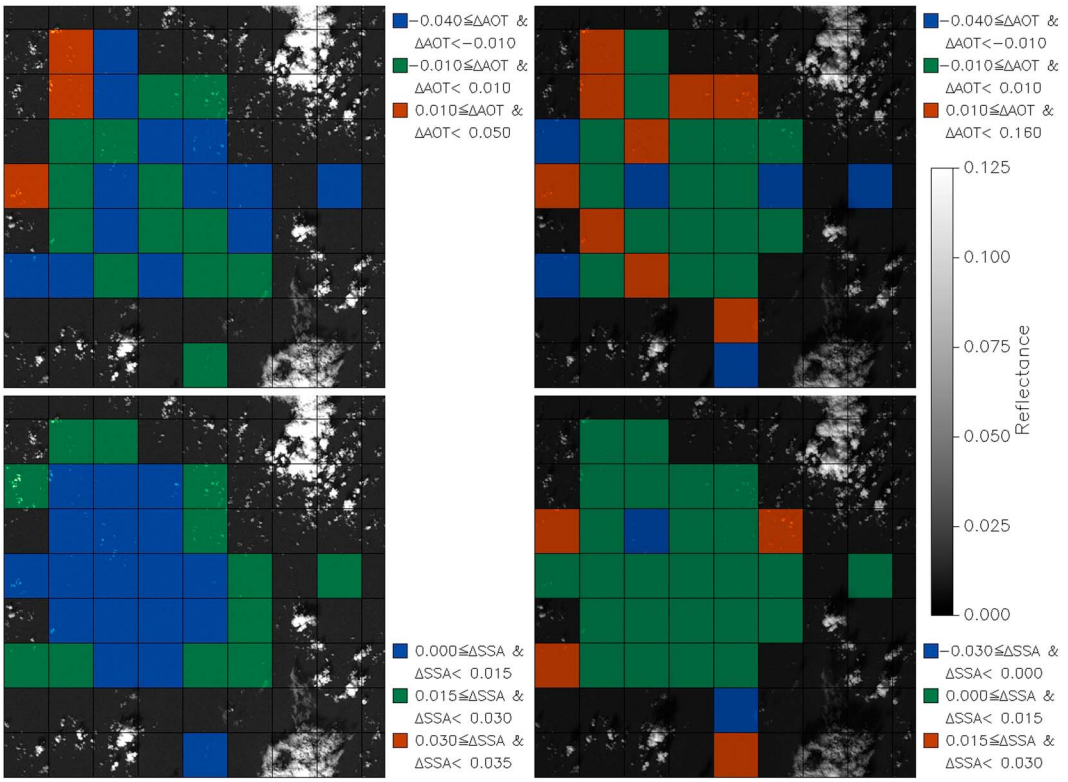

Figure 16. The same as Figure 13 except that this retrieval excludes the 410 nm band.

21698996, 2016, 21, Downloaded from https://agupubs.onlinelibrary.wiley.com/doi/10.1002/2016JD024787, Wiley Online Library on [24/02/2025]. See the Terms and Conditions (https://onlinelibrary.wiley.com/terms-and-conditions) on Wiley Online Library for rules of use; OA articles are governed by the applicable Creative Commons License

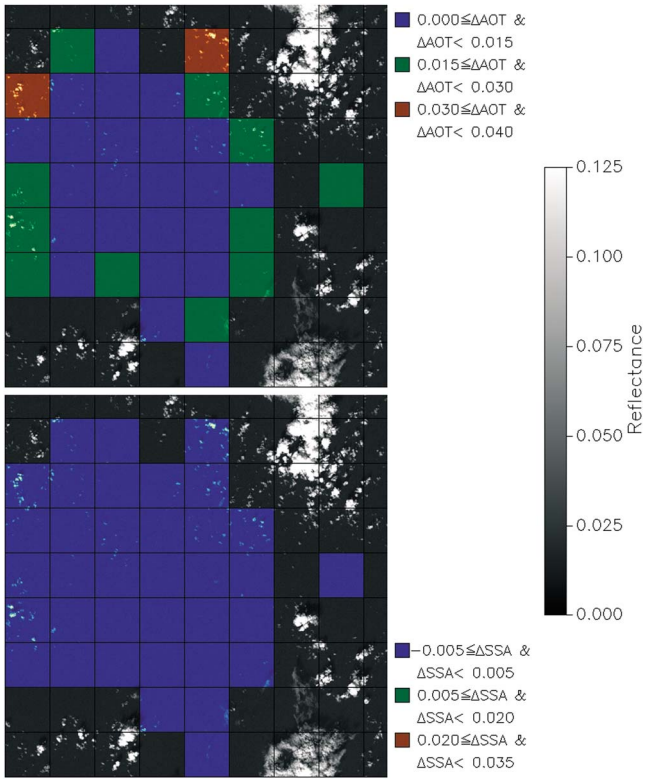

Figure 17. The bias in the retrieved total (top) AOT and (bottom) SSA for the simultaneous aerosol and cloud retrievals with $\chi^2 \leq 2.0$ in the scene with cloud distribution of case A, the fine nonabsorbing aerosol (type C), and SZA = 40°.

reduced compared to the results of Figure 13. It should be noted, however, that apart from 3-D effects close to clouds, near-UV measurements provide important information about aerosols, in particular on aerosol absorption and aerosol layer height. Our study shows that in the neighborhood of clouds aerosol retrievals using these wavelengths should be interpreted with care, if 3-D effects are not accounted for in the retrieval.

3.5.4. Effect of Aerosol Absorption

The effects of the 3-D radiance enhancement are different for aerosol type C which consists of aerosols that are virtually nonabsorbing. Figure 17 shows the errors on AOT and SSA due to 3-D effects for this aerosol type. It can be seen that now the radiance enhancement causes an overestimation of the AOT while the SSA is practically unaffected. This may be explained by the fact that for this aerosol type the radiance enhancement cannot be compensated by a larger SSA, because SSA obviously has an upper boundary of 1.0. So different than for the absorbing aerosol type, for the nonabsorbing case it is most effective to compensate 3-D radiance enhancements by an increase in retrieved AOT.

4. Conclusion

We have investigated the performance of multiangle, multiwavelength photopolarimetric retrievals in scenes with partial, liquid water cloud cover and scenes in the vicinity of liquid water clouds. For this purpose, we have created synthetic, multiangle, multiwavelength photopolarimetric observations of scenes with realistic, liquid water clouds from a LES model using a 3-D RT model. In particular, our aim was to address the following research questions.

4.1. What is the Capability of Aerosol-Only Retrievals From Multiangle Photopolarimetric Measurements to Provide Aerosol Information in the Vicinity of Clouds?

Our study confirms that multiangle photopolarimetric measurements can efficiently filter out cloud contamination using a goodness-of-fit criterion, as was found empirically by *Stap et al.* [2015] using POLDER-3 measurements. So, in general, cloud-contaminated measurements cannot be reproduced using a forward model that only includes aerosol parameters. A goodness-of-fit criterion also filters out scenes in the vicinity of clouds where geometrical 3-D radiative effects are present. In some cases with little cloud

21698996, 2016, 21, Downloaded from https://agupubs.onlinelibrary.wiley.com/doi/10.1002/2016JD024787, Wiley Online Library on [24/02/2025]. See the Terms and Conditions (https://onlinelibrary.wiley.com/terms-and-conditions) on Wiley Online Library for rules of use; OA articles are governed by the applicable Creative Commons License

21698996, 2016, 21, Downloaded from https://agupubs.onlinelibrary.wiley.com/doi/10.1002/2016JD024787, Wiley Online Library on [24/02/2025]. See the Terms and Conditions (https://onlinelibrary.wiley.com/terms-and-conditions) on Wiley Online Library for rules of use; OA articles are governed by the applicable Creative Commons License

contamination we found that a good fit can be obtained but for those cases the retrieved aerosol parameters were affected only by a small amount due to the cloud contamination. So in the overall data set the errors in the retrieved AOT, effective radii, and real parts of the refractive indices are biased due to 3-D radiative effects and cloud contamination, but, in general, this bias is smaller than the accuracy requirements formulated by *Mishchenko et al.* [2004]. However, under certain conditions the 3-D effects are such that retrieval errors on the retrieved AOT and SSA are larger than these requirements. The overestimate in the SSA can be larger than the accuracy requirements depending on the cloud distribution and aerosol model (also see Table 5). The underestimate in AOT is, in general, within the accuracy requirement, but small trends are found as function of cloud contamination. These trends may hamper studies on aerosol-cloud relationships.

4.2. Can Aerosol Retrievals in the Vicinity of Clouds be Improved When Cloud Properties are Fitted Simultaneously With Aerosol Properties?

We have performed simultaneous aerosol-cloud retrievals from the synthetic data set, where we retrieve cloud fraction and optical thickness in addition to the parameters of a bimodal aerosol model. These simultaneous aerosol-cloud retrievals were performed using a forward model based on 1-D radiative transfer. We found that the aerosol-cloud retrievals are able to provide a good fit to the measurements in more cases with partial cloud cover, yielding more valid retrievals in the vicinity of clouds. Also, the AOT trend that was found for aerosol-only retrievals between cloud-free and cloud-contaminated scenes is virtually absent for combined aerosol-cloud retrievals.

However, like for the aerosol-only retrievals, the retrieved aerosol retrievals in cloud-free scenes are affected by 3-D radiance enhancements caused by neighboring clouds. In most cases the resulting errors are within the accuracy requirements formulated by *Mishchenko et al.* [2004]. For absorbing aerosols the most prominent 3-D-induced error is an underestimate in AOT combined with an overestimate in SSA for scenes with radiance enhancements because of 3-D scattering by clouds. For aerosols that are practically nonabsorbing, we find for those scenes that the AOT is overestimated while the SSA is virtually unaffected. It is important to note that the AOT bias induced by 3-D radiative transfer effect is smaller than the expected effect of aerosol swelling near clouds due to water uptake [*Koren et al.*, 2007]. Because 3-D radiance enhancements are strongest at blue/near-UV wavelengths, AOT and SSA are slightly reduced for retrievals that do not make use of the 410 nm band. This is in particular the case for regions where the 3-D radiance enhancements dominate over 3-D geometrical effects. It should be noted, however, that apart from 3-D effects close to clouds, near-UV measurements provide important information about aerosols, in particular on aerosol absorption and aerosol layer height.

Overall, aerosol retrievals in the vicinity of clouds can be improved, in particular in terms of data coverage, by fitting cloud properties simultaneously with aerosol properties using a 1-D radiative transfer model. To reduce the remaining (overall small) biases caused by 3-D radiative enhancements, and to extend coverage to areas where geometrical 3-D effects dominate, RT models used in retrieval algorithms have to be extended to account for 3-D effects [*Martin et al.*, 2014; *Marshak et al.*, 2014].

4.3. What Is the Benefit of Improved Spatial Resolution for Aerosol Retrievals in the Vicinity of Clouds?

We performed aerosol-only and simultaneous aerosol-cloud retrievals for generic satellite observations with spatial resolutions of 2×2, 4×4, and 6×6 km^2. For both the aerosol-only retrievals and simultaneous aerosol-cloud retrievals we found that we cannot obtain aerosol retrievals closer to clouds for the highest (2×2 km^2) spatial resolution. The main reason for this is that 3-D geometric effects hamper a good fit of the 1-D forward model to the 3-D synthetic measurements. Since the 3-D geometric effects are less pronounced for the lowest spatial resolution (6×6 km^2), we found that the simultaneous aerosol-cloud retrieval works significantly better at this spatial resolution. We conclude that to exploit the additional value of higher spatial resolution measurements (2×2 km^2 or higher in the vicinity of clouds), 3-D radiative transfer effects have to be explicitly accounted for in the retrieval algorithm.

Acknowledgments

The authors would like to thank A. Seifert for providing the RICO data and Tobias Zinner for his help with interpreting it. The synthetic measurements generated in this study can be obtained by sending an e-mail request to O.Hasekamp@sron.nl.

References

Albrecht, B. A. (1989), Aerosols, cloud microphysics, and fractional cloudiness, *Science*, *245*, 1227–1230, doi:10.1126/science.245.4923.1227.

Bellouin, N., J. Quaas, J.-J. Morcrette, and O. Boucher (2013), Estimates of aerosol radiative forcing from the MACC re-analysis, *Atmos. Chem. Phys.*, *13*, 2045–2062, doi:10.5194/acp-13-2045-2013.

Boucher, O., et al. (2013), Clouds and Aerosols, in *Climate Change 2013: The Physical Science Basis. Contribution of Working Group I to the Fifth Assessment Report of the Intergovernmental Panel on Climate Change*, edited by T. F. Stocker et al., 1535 pp., Cambridge Univ. Press, Cambridge, U. K., and New York.

Bréon, F.-M., D. Tanré, and S. Generoso (2002), Aerosol effect on cloud droplet size monitored from satellite, *Science*, *295*, 834–838, doi:10.1126/science.1066434.

Buras, R., and B. Mayer (2011), Efficient unbiased variance reduction techniques for Monte Carlo simulations of radiative transfer in cloudy atmospheres: The solution, *J. Quant. Spectrosc. Ra.*, *112*, 434–447, doi:10.1016/j.jqsrt.2010.10.005.

Charlson, R. J., A. S. Ackerman, F. A.-M. Bender, T. L. Anderson, and Z. Liu (2007), On the climate forcing consequences of the albedo continuum between cloudy and clear air, *TELLUS B*, *59*, 715–727, doi:10.1111/j.1600-0889.2007.00297.x.

Chowdhary, J., B. Cairns, M. I. Mishchenko, P. V. Hobbs, G. F. Cota, J. Redemann, K. Rutledge, B. N. Holben, and E. Russell (2005), Retrieval of aerosol scattering and absorption properties from photopolarimetric observations over the ocean during the CLAMS experiment, *J. Atmos. Sci.*, *62*, 1093–1117, doi:10.1175/JAS3389.1.

Di Noia, A., O. P. Hasekamp, G. van Harten, J. H. H. Rietjens, J. M. Smit, F. Snik, J. S. Henzing, J. de Boer, C. U. Keller, and H. Volten (2015), Use of neural networks in ground-based aerosol retrievals from multi-angle spectropolarimetric observations, *Atmos. Meas. Tech.*, *8*, 281–299, doi:10.5194/amt-8-281-2015.

Dubovik, O., et al. (2006), Application of spheroid models to account for aerosol particle nonsphericity in remote sensing of desert dust, *J. Geophys. Res.*, *111*, D11208, doi:10.1029/2005JD006619.

Emde, C., and B. Mayer (2007), Simulation of solar radiation during a total eclipse: A challenge for radiative transfer, *Atmos. Chem. Phys.*, *7*, 2259–2270.

Emde, C., R. Buras, B. Mayer, and M. Blumthaler (2010), The impact of aerosols on polarized sky radiance: Model development, validation, and applications, *Atmos. Chem. Phys.*, *10*, 383–396.

Emde, C., et al. (2016), The libRadtran software package for radiative transfer calculations (version 2.0.1), *Geosci. Model Dev.*, *9*, 1647–1672, doi:10.5194/gmd-9-1647-2016.

Hansen, J. E., and L. D. Travis (1974), Light scattering in planetary atmospheres, *Space Sci. Rev.*, *16*, 527–610, doi:10.1007/BF00168069.

Hasekamp, O. P. (2010), Capability of multi-viewing-angle photo-polarimetric measurements for the simultaneous retrieval of aerosol and cloud properties, *Atmos. Meas. Tech.*, *3*, 839–851.

Hasekamp, O. P., and J. Landgraf (2002), A linearized vector radiative transfer model for atmospheric trace gas retrieval, *J. Quant. Spectrosc. Ra.*, *75*, 221–238, doi:10.1016/S0022-4073(01)00247-3.

Hasekamp, O. P., and J. Landgraf (2005), Linearization of vector radiative transfer with respect to aerosol properties and its use in satellite remote sensing, *J. Geophys. Res.*, *110*, D04203, doi:10.1029/2004JD005260.

Hasekamp, O. P., and J. Landgraf (2007), Retrieval of aerosol properties over land surfaces: Capabilities of multiple-viewing-angle intensity and polarization measurements, *Appl. Optics*, *46*, 3332–3344, doi:10.1364/AO.46.003332.

Hasekamp, O. P., P. Litvinov, and A. Butz (2011), Aerosol properties over the ocean from PARASOL multiangle photopolarimetric measurements, *J. Geophys. Res.*, *116*, D14204, doi:10.1029/2010JD015469.

Knobelspiesse, K., B. Cairns, M. Mishchenko, J. Chowdhary, K. Tsigaridis, B. van Diedenhoven, W. Martin, M. Ottaviani, and M. Alexandrov (2012), Analysis of fine-mode aerosol retrieval capabilities by different passive remote sensing instrument designs, *Opt. Express*, *20*, 21457–21484, doi:10.1364/OE.20.021457.

Kokhanovsky, A. A., et al. (2010), The inter-comparison of major satellite aerosol retrieval algorithms using simulated intensity and polarization characteristics of reflected light, *Atmos. Meas. Tech.*, *3*, 909–932.

Koren, I., L. A. Remer, Y. J. Kaufman, Y. Rudich, and J. V. Martins (2007), On the twilight zone between clouds and aerosols, *Geophys. Res. Lett.*, *34*, L08805, doi:10.1029/2007GL029253.

Landgraf, J., O. P. Hasekamp, M. A. Box, and T. Trautmann (2001), A linearized radiative transfer model for ozone profile retrieval using the analytical forward-adjoint perturbation theory approach, *J. Geophys. Res.*, *106*, 27291–27305, doi:10.1029/2001JD000636.

Lohmann, U., and J. Feichter (2005), Global indirect aerosol effects: A review, *Atmos. Chem. Phys.*, *5*, 715–737.

Lohmann, U., and G. Lesins (2002), Stronger constraints on the anthropogenic indirect aerosol effect, *Science*, *298*, 1012–1015, doi:10.1126/science.1075405.

Marshak, A., and A. Davis (2005), *3D Radiative Transfer in Cloudy Atmospheres*, Physics of Earth and Space Environments, Springer, New York.

Marshak, A., K. F. Evans, T. Varnai, and G. Wen (2014), Extending 3D near-cloud corrections from shorter to longer wavelengths, *J. Quant. Spectrosc. Ra.*, *147*, 79–85, doi:10.1016/j.jqsrt.2014.05.022.

Martin, W., B. Cairns, and G. Bal (2014), Adjoint methods for adjusting three-dimensional atmosphere and surface properties to fit multi-angle/multi-pixel polarimetric measurements, *J. Quant. Spectrosc. Ra.*, *144*, 68–85, doi:10.1016/j.jqsrt.2014.03.030.

Mayer, B. (2009), Radiative transfer in the cloudy atmosphere, *Eur. Phys. J. Conf.*, *1*, 75–99, doi:10.1140/epjconf/e2009-00912-1.

Mishchenko, M. I., and L. D. Travis (1997), Satellite retrieval of aerosol properties over the ocean using polarization as well as intensity of reflected sunlight, *J. Geophys. Res.*, *102*, 16989–17013, doi:10.1029/96JD02425.

Mishchenko, M. I., B. Cairns, J. E. Hansen, L. D. Travis, R. Burg, Y. J. Kaufman, J. Vanderlei Martins, and E. P. Shettle (2004), Monitoring of aerosol forcing of climate from space: Analysis of measurement requirements, *J. Quant. Spectrosc. Ra.*, *88*, 149–161, doi:10.1016/j.jqsrt.2004.03.030.

Nakajima, T., and M. Tanaka (1988), Algorithms for radiative intensity calculations in moderately thick atmospheres using a truncation approximation, *J. Quant. Spectrosc. Ra.*, *40*, 51–69, doi:10.1016/0022-4073(88)90031-3.

Ottaviani, M., K. Knobelspiesse, B. Cairns, and M. Mishchenko (2013), Information content of aerosol retrievals in the sunglint region, *Geophys. Res. Lett.*, *40*, 631–634, doi:10.1002/grl.50148.

Quaas, J., O. Boucher, and U. Lohmann (2006), Constraining the total aerosol indirect effect in the LMDZ and ECHAM4 GCMs using MODIS satellite data, *Atmos. Chem. Phys.*, *6*, 947–955.

Quaas, J., O. Boucher, N. Bellouin, and S. Kinne (2008), Satellite-based estimate of the direct and indirect aerosol climate forcing, *J. Geophys. Res.*, *113*, D05204, doi:10.1029/2007JD008962.

Rauber, R. M., et al. (2007), Rain in shallow cumulus over the ocean, *Bull. Am. Meteorol. Soc.*, *88*, 1912–1928, doi:10.1175/BAMS-88-12-1912.

Redemann, J., Q. Zhang, P. B. Russell, J. M. Livingston, and L. A. Remer (2009), Case studies of aerosol remote sensing in the vicinity of clouds, *J. Geophys. Res.*, *114*, D06209, doi:10.1029/2008JD010774.

Segelstein, D. J. (1981), *The Complex Refractive Index of Water*, Department of Physics, University of Missouri, Kansas, Mo.

Seifert, A., and T. Heus (2013), Large-eddy simulation of organized precipitating trade wind cumulus clouds, *Atmos. Chem. Phys.*, *13*, 5631–5645, doi:10.5194/acp-13-5631-2013.

Sekiguchi, M., T. Nakajima, K. Suzuki, K. Kawamoto, A. Higurashi, D. Rosenfeld, I. Sano, and S. Mukai (2003), A study of the direct and indirect effects of aerosols using global satellite data sets of aerosol and cloud parameters, *J. Geophys. Res.*, *108*, 4699, doi:10.1029/2002JD003359.

21698996, 2016, 21, Downloaded from https://agupubs.onlinelibrary.wiley.com/doi/10.1002/2016JD024787, Wiley Online Library on [24/02/2025]. See the Terms and Conditions (https://onlinelibrary.wiley.com/terms-and-conditions) on Wiley Online Library for rules of use; OA articles are governed by the applicable Creative Commons License

Stap, F. A., O. P. Hasekamp, and T. Röckmann (2015), Sensitivity of PARASOL multi-angle photopolarimetric aerosol retrievals to cloud contamination, *Atmos. Meas. Tech.*, *8*, 1287–1301, doi:10.5194/amt-8-1287-2015.

Stap, F. A., O. P. Hasekamp, C. Emde, and T. Röckmann (2016), Influence of 3D effects on 1D aerosol retrievals in synthetic, partially clouded scenes, *J. Quant. Spectrosc. Ra.*, *170*, 54–68, doi:10.1016/j.jqsrt.2015.10.008.

Stevens, B., C.-H. Moeng, and P. P. Sullivan (1999), Large-eddy simulations of radiatively driven convection: Sensitivities to the representation of small scales, *J. Atmos. Sci.*, *56*, 3963–3984, doi:10.1175/1520-0469(1999)056<3963:LESORD>2.0.CO;2.

Stevens, B., et al. (2005), Evaluation of large-eddy simulations via observations of nocturnal marine stratocumulus, *Mon. Weather Rev.*, *133*, 1443, doi:10.1175/MWR2930.1.

Stevens, B., and A. Seifert (2008), Understanding macrophysical outcomes of microphysical choices in simulations of shallow cumulus convection, *J. Meteorol. Soc. Jpn. Ser. II*, *86A*, 143–162, doi:10.2151/jmsj.86A.143.

Twomey, S. (1959), The nuclei of natural cloud formation. Part I: The chemical diffusion method and its application to atmospheric nuclei, *Geofis. Pura Appl.*, *43*, 227–242, doi:10.1007/BF01993559.

Várnai, T., and A. Marshak (2009), MODIS observations of enhanced clear sky reflectance near clouds, *Geophys. Res. Lett.*, *36*, L06807, doi:10.1029/2008GL037089.

Waquet, F., B. Cairns, K. Knobelspiesse, J. Chowdhary, L. D. Travis, B. Schmid, and M. I. Mishchenko (2009), Polarimetric remote sensing of aerosols over land, *J. Geophys. Res.*, *114*, D01206, doi:10.1029/2008JD010619.

Wen, G., A. Marshak, R. F. Cahalan, L. A. Remer, and R. G. Kleidman (2007), 3-D aerosol-cloud radiative interaction observed in collocated MODIS and ASTER images of cumulus cloud fields, *J. Geophys. Res.*, *112*, D13204, doi:10.1029/2006JD008267.

Wu, L., O. Hasekamp, B. van Diedenhoven, and B. Cairns (2015), Aerosol retrieval from multiangle, multispectral photopolarimetric measurements: Importance of spectral range and angular resolution, *Atmos. Meas. Tech.*, *8*, 2625–2638, doi:10.5194/amt-8-2625-2015.

21698996, 2016, 21, Downloaded from https://agupubs.onlinelibrary.wiley.com/doi/10.1002/2016JD024787, Wiley Online Library on [24/02/2025]. See the Terms and Conditions (https://onlinelibrary.wiley.com/terms-and-conditions) on Wiley Online Library for rules of use; OA articles are governed by the applicable Creative Commons License